Quantum Well Solar Cells: Principles, Recent Progress, and Potential

Islam Sayed ⬤, *Member, IEEE*, and S. M. Bedair, *Fellow, IEEE*

Abstract—**Quantum well solar cells, as a promising approach for next-generation photovoltaic technology, have received great attention in the last few years. Recent developments in materials growth and device structures of quantum wells have opened up new avenues for the incorporation of quantum well structures in next-generation III/V multi-junction solar cells. In this paper, the advantages and challenges of growing quantum wells in the unintentionally doped (i) region of p-i-n solar cells are reviewed. We focus on the recent progress in 1.1–1.3 eV strain-balanced In-GaAs/GaAsP, 1.6–1.8 eV strain-balanced and lattice-matched In-GaAsP/InGaP, and >2.1 eV strained InGaN/GaN quantum well solar cells, including optimization of the quantum well growth conditions and improving the solar cell structure. For each material system, the challenges associated with materials growth and device performance such as critical layer thickness constraints, strain balance, bandgap tunability, and carrier transport limitations, are discussed. The performance of each quantum well solar cell is compared with bulk absorber operating in the same bandgap range, with the advantages of each being highlighted. The effect of the unintentional background doping on carrier collection (by drift) is presented through modeling and recent experimental results. The recent strategies to enhance the electric field distribution across the quantum well region are reviewed. The potential of incorporating quantum well structures in next-generation multi-junction devices is also discussed.**

Index Terms—**III–V, bandgap engineering, GaAs, GaN, InGaAsP, InGaP, multi-junction solar cells, quantum wells (QWs), solar cells.**

I. INTRODUCTION

THERE has been an intensive search for high-efficiency photovoltaics since the invention of the first p-n silicon solar cells in the 1950 s [1]. Among all alternative photovoltaic technologies, the III/V multi-junction solar cells are the most efficient photovoltaic technology nowadays with demonstrated efficiency (η) of 46% under high solar concentration [2], [3]. The multi-junction solar cells concept relies on stacking p-n junctions with different bandgaps, each tuned to absorb different windows of the solar spectrum. The first multi-junction solar cell was based on $Al_{0.2}Ga_{0.8}As$/GaAs dual-junction and was demonstrated in 1979 [4]. Inverted metamorphic (IMM) In-GaAsP/InGaAs and lattice-matched InGaP/GaAs dual-junction have recently realized one-sun efficiencies of 32.6% [5] and 32.8% [6], respectively. Lattice-matched InGaP/Ga(In)As/Ge and IMM InGaP/GaAs/InGaAs triple-junction solar cells have realized η of 44.0% and 44.4% [7], [8], respectively, under high solar concentration. Quadruple-junction wafer-bonded [2] and IMM [3] structures have demonstrated η of ∼46%, under high solar concentration. Next generation multi-junction devices will have five (or more) junctions with prospective η exceeding 50% under high solar concentration [9], [10].

The realization of the ideal subcells with optimal bandgaps (E_g) in current and next-generation III–V solar cells is challenged by the relation between the bandgap and lattice constant of materials. Subcells with optimal bandgaps, as indicated by modeling [11]–[15], typically do not have the same lattice constants. Direct growth of materials with different lattice constants result in detrimental dislocations [16], which reduce the diffusion length and carrier lifetime [17], resulting in an increased dark current, and reduced open-circuit voltage (V_{oc}), fill factor (FF), and η [18], [19]. In addition, series-connected two-terminal multi-junction solar cell designs seek to have an excellent current match between subcells or add more subcells to divide the solar spectrum evenly [20], [21]. Hence, an ideal multi-junction solar cell will have minimal defects with the identical current generated from each subcell. There are three main approaches to overcome the material quality and lattice-matching limitations: wafer bonding, metamorphic growth, and the inclusion of quantum wells (QWs). First, the wafer bonding approach employs combining structures of different lattice constants grown on different substrates. One example of wafer bonding is InGaP (1.88 eV)/GaAs (1.42 eV)//InGaAsP (1.12 eV)/InGaAs (0.74 eV) four-junction (4J) solar cell [2], where lattice-matched InGaP/GaAs and InGaAsP/InGaAs structures were grown separately on GaAs and InP substrates, respectively. Then, the two junctions are bonded to each other during processing and the GaAs substrate is lifted-off. Second, the metamorphic growth approach uses a compositionally graded buffer to relieve the build-up of stress during monolithic growth in order to access subcells with optimal bandgaps that cannot be epitaxially grown without defects [22], [23]. One example of a metamorphic structure is 4J InGaP (1.8 eV)/GaAs (1.40 eV)/InGaAs (1.0 eV)/InGaAs (0.7 eV), where a compositionally graded
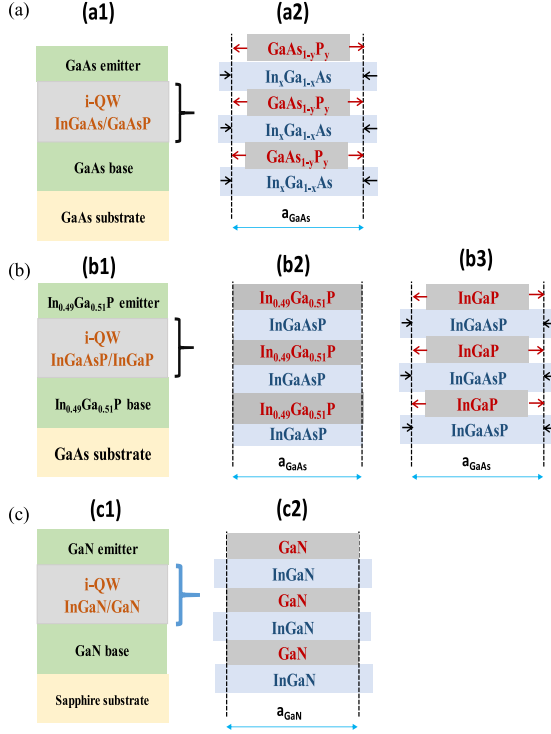
Fig. 1. Schematics of (a) GaAs p-i-n solar cell that includes strain-balanced InGaAs/GaAsP quantum wells, grown on GaAs substrate. (b) $In_{0.49}Ga_{0.51}P$ p-i-n solar cell that includes lattice-matched $In_xGa_{1-x}As_{1-z}P_z/In_{0.49}Ga_{0.51}P$ ($x \sim (0.08 + z)/2.08$ [30]; $0 \leq x \leq 1$ and $0 \leq z \leq 1$) or strain-balanced InGaAsP/InGaP quantum wells, grown on GaAs substrate. (c) GaN p-i-n solar cell that includes strained InGaN/GaN quantum wells, grown on GaN templates on sapphire substrate. The range of compositions used for each material system is discussed in the text. The well/barrier thicknesses, as well as the compositions, are adjusted to strain-balance the InGaAs/GaAsP and InGaAsP/InGaP QW structures as discussed in detail in Section III-C.

transparent buffer of InGaP was grown to reduce the introduction of dislocations between InGaAs and GaAs subcells [23].

The use of QWs is an alternative promising approach to realize multi-junction solar cell structures with optimal bandgaps and lattice mismatched materials without generating excessive dislocations [24]–[29]. QWs are periodic nanostructures that consist of a low bandgap material, well, sandwiched between two higher bandgaps, barriers. Schematics of the three QW structures, studied in this article, are shown in Fig. 1. The InGaAs/GaAsP, InGaAsP/InGaP, and InGaN/GaN QWs are grown in the intrinsic region of p-i-n (or n-i-p) solar cell structures, as shown in the schematics of Fig. 1. The emitter/base of InGaAs/GaAsP, InGaAsP/InGaP, and InGaN/GaN QW solar cells are GaAs, $In_{0.49}Ga_{0.51}P$, and GaN, respectively, as shown in Fig. 1.

This paper discusses the advantages and challenges of growing QWs in p-i-n solar cells. In Section II, the different QW approaches are summarized. The design factors that challenge the realization of high-performance quantum well solar cells (QWSC) devices such as critical layer thickness (CLT), strain-balance, and carrier transport are discussed in Section III. The recent progress in 1.1–1.3 eV InGaAs/GaAsP, 1.6–1.8 eV InGaAsP/InGaP, and >2.1 eV InGaN/GaN QWSC, is discussed

in Section IV. Then, a comparison between the performances of QWSC and bulk absorbers operating in the same bandgap range is conducted in Section V, with the challenges of each approach is being highlighted. The effect of the unintentional background doping in the QW region on the electric field distribution is studied with the aid of modeling results in Section VI. Recent efforts to enhance the carrier collection (by drift) through obtaining a uniform electric field distribution across the QW region, are reviewed in Section VI as well. The challenges and potential of QW structures in multi-junction solar cells are discussed in Section VII. The purpose of this paper is to present a detailed review of the present QWs for potential use in multi-junction solar devices in the context of the recent results with a future guideline.

II. QUANTUM WELL MATERIAL SYSTEM AND DEVICE STRUCTURES

The QWs can be either lattice-matched, strain-balanced, or strained as shown in Fig. 1 using the appropriate range of compositions. The lattice constant-bandgap diagram of each QW structure, showing the well/barrier lattice constants and bandgap range for each material system is shown in Fig. 2.

The first QW approach is the lattice-matched material systems, where the well and barrier have lattice-constants similar to the underlying substrate. For example, $In_xGa_{1-x}As_{1-z}P_z$ well and $In_{0.49}Ga_{0.51}P$ barrier can be grown lattice-matched to GaAs substrates, in the intrinsic region (i) of $In_{0.49}Ga_{0.51}P$ p-i-n solar cells, where $x \sim (0.08 + z)/2.08$ [30]; $0 \leq x \leq 1$ and $0 \leq z \leq 1$. The second QW approach is the strain-balanced material systems, where psudeomorphically layers are epitaxially grown through balancing the compressive stress formed by the well with the tensile stress on the barrier, as shown in Fig. 1(a2) and (b3). Examples of strain-balanced material systems are InGaAs/GaAsP and InGaAsP/InGaP grown in the intrinsic region of GaAs p-i-n and $In_{0.49}Ga_{0.51}P$ p-i-n structures as shown in Fig. 1(a2) and (b3), respectively. For the strain-balanced InGaAs/GaAsP QW system, the InGaAs QW was grown under compressive stress, with lattice constant higher than that of GaAs, to tune the bandgap to less than 1.4 eV, as shown in Fig. 2(a). The well and barrier thicknesses, as well as the compositions, are adjusted to strain-balance the structure as will be discussed in detail in Section III-C. There is a wide range of compositions and thicknesses that can lead to a strain-balanced material system, thus offering a great design flexibility for solar cell designers. For example, an $In_{0.11}Ga_{0.89}As$ well with a thickness of 93 Å can be strain-balanced with a $GaAs_{0.93}P_{0.07}$ barrier with a thickness of 160 Å, as shown by Adams et al. [31]. Also, a 115 Å $In_{0.14}Ga_{0.86}As$ well can be strain-balanced with a 27 Å $GaAs_{0.24}P_{0.76}$ barrier as shown by Bradshaw et al. [32]. The choice of compositions and thicknesses depends on many factors such as strain-balance, bandgap requirements, and carrier transport limitations, as will be discussed in detail in Sections III and IV. For the strain-balanced InGaAsP/InGaP QW system, InGaAsP is grown with indium composition of higher than 49%, to tune the bandgap of $In_{0.49}Ga_{0.51}P$-based cells (1.85 eV) to the 1.6–1.8 eV range as shown in Fig. 2(b).
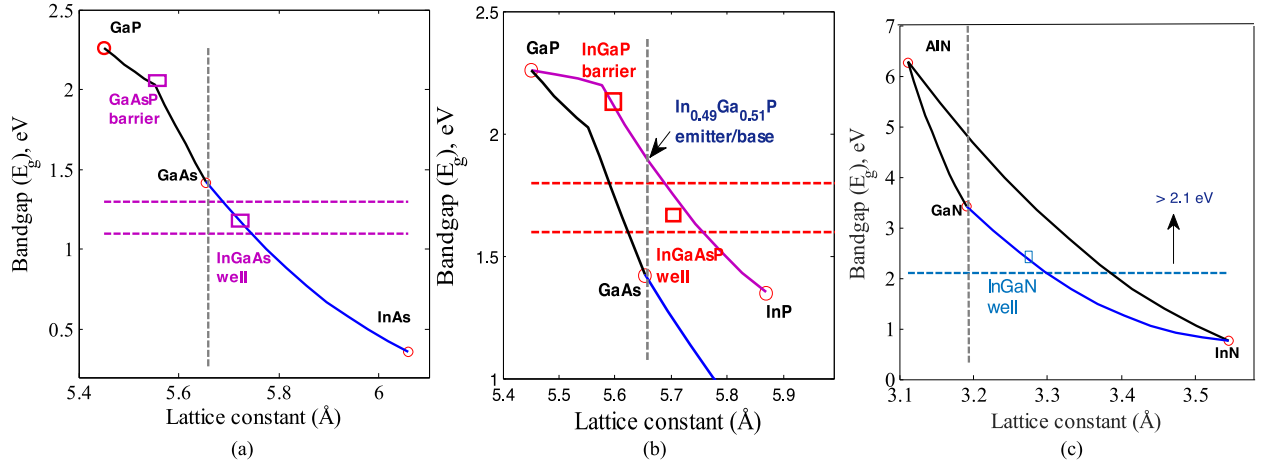
Fig. 2. Bandgap versus lattice constants showing the well and barrier compositions for the three QW structures in Fig. 1. (a) Strain-balanced InGaAs/GaAsP QWs. (b) Strain-balanced InGaAsP/InGaP QWs. (c) Strained InGaN/GaN QWs. The vertical dotted line in each figure represents the lattice-matched condition to GaAs/GaN. The horizontal dotted lines represent the region of interest in each QW structure for various multi-junction solar cell designs. For the InGaAs/GaAsP and InGaAsP/InGaP QW structures, well/barrier thicknesses, as well as the compositions, are adjusted to achieve strain-balanced structures as discussed in detail in Section III-C.

Using the strain-balance concept, the build-up of strain energy during growth can be controlled, in order to allow the growth of a high number of periodic QWs with minimal stress relaxation. This concept was developed, by Bedair *et al.*, in the 1980s in light-emitting diodes (LEDs) to tune the bandgap of GaAs to lower energy values [33]. Then, the same concept was applied to solar cells [26], [28] to provide more design flexibility in tuning subcells in multi-junction devices. The third QW approach is the strained material system, where the lattice constants of the well and barrier are not similar as shown in Figs. 1(c2) and 2(c) for the InGaN/GaN material system. This results in a strained structure and the net stress in the whole structure will be compressive, which will limit the number of QWs that can be included in any GaN n-i-p structure. The strained InGaN/GaN QW tune the bandgap to energy values less than 3.4 eV as shown in Fig. 2(c). Using the QW approach, strain-balanced InGaAs/GaAsP on GaAs substrates [25], [28], [31], [32], [34]–[40], strain-balanced and lattice-matched InGaAsP/InGaP on GaAs substrates [35], [41]–[43], and strained InGaN/GaN grown on GaN templates on sapphire substrates [44]–[50] have been proposed as alternatives to realize 1.1–1.3 eV, 1.6–1.8 eV, and >2.1 eV solar cells, respectively, as shown in Fig. 2.

III. PRINCIPLES OF QUANTUM WELL SOLAR CELLS

The challenges for the realization of high-performance QWSCs are mainly materials growth with high-quality and realizing efficient light absorption and carrier collection. These challenges will be discussed by modeling the bandgap tunability, CLT, and strain-balance constraints of InGaAs/GaAsP, InGaAsP/InGaP, and InGaN/GaN. The effects of layers thicknesses and compositions on carrier collection (by drift) are also discussed.

A. Bandgap Tunability

As shown in the lattice-constant versus bandgap diagrams of Fig. 2(a) and (b), the strain-balance approach allows one to

optimally select the bandgap of each junction to maximize the efficiency of multi-junction solar cells. For example, the use of strain-balanced InGaAs/GaAsP QWs allows one to access absorbing layers in the 1.1–1.3 eV range, which are not available from a bulk material lattice matched to GaAs, as shown in Fig. 2(a). This can be achieved while maintaining the lattice-matching condition to GaAs substrates. The effective bandgap ($E_{G,\mathrm{Eff}}$), or equivalently the optical absorption threshold, of a QW structure is a function of quantum size effects (QSE), quantum confined stark effects (QCSE), and stress effects. Thus, the $E_{G,\mathrm{Eff}}$ of these QW structures should be adjusted to account for current-matching condition in the multi-junction solar cell structure.

The $E_{G,\mathrm{Eff}}$ of the QW can be estimated as follows:

$$E_{G,\mathrm{Eff}} = E_G^{\mathrm{well,relaxed}} + \Delta E_G^{\mathrm{Strain}} + \Delta E_G^{\mathrm{QSE}} + \Delta E_G^{\mathrm{QCSE}} \tag{1}$$

where $E_G^{\mathrm{well, relaxed}}$ represents the relaxed well bandgap, $\Delta E_G^{\mathrm{Strain}}$ represents the shift in the QWs absorption due to compressive or tensile strain in the multiple-quantum well layers, $\Delta E_G^{\mathrm{QSE}}$ represents the bandgap shift due to the QSE [51], and $\Delta E_G^{\mathrm{QCSE}}$ represents the well thickness-dependent shift in the effective band gap due to QCSE [52], [53]. The bandgaps used in the model for InGaAs, GaAsP, InGaAsP, InGaP, and InGaN are linearly interpolated between the binary compounds [54]. The conduction band and valence band offsets are estimated based on the Anderson's rule (electron affinity rule) [55]. Kronig–Penney model is used to calculate the quantum states [51]. The strain has two effects on the band gap. The first effect is a change in the relative energy of the conduction and valence band energy. The magnitude of this energy difference, ΔE, depends upon the strain, ε, the elastic stiffness' coefficients, C_{11} and C_{12}, and the hydrostatic deformation potential, "a". These parameters depend upon the composition of the strained layer
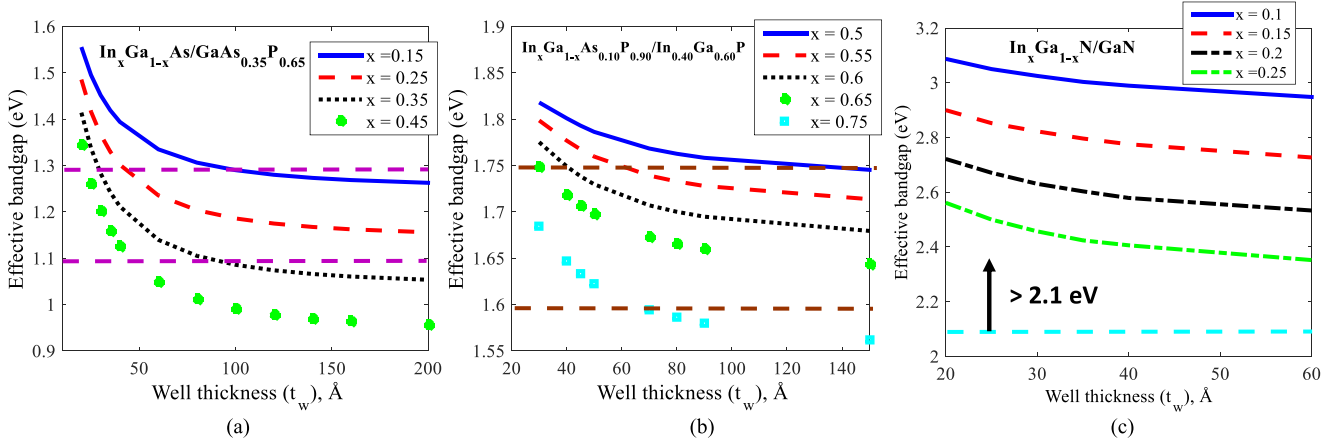
Fig. 3. Effective bandgap versus well thickness (t_w) for various indium compositions, x, in wells for the following structures. (a) Strain-balanced $In_xGa_{1-x}As/GaAs_{0.35}P_{0.65}$. (b) Strain-balanced $In_xGa_{1-x}As_{0.10}P_{0.90}/In_{0.40}Ga_{0.60}P$. (c) Strained $In_xGa_{1-x}N/GaN$. The barrier thickness (t_b) of $GaAs_{0.35}P_{0.65}$ and $In_{0.40}Ga_{0.60}P$ were adjusted to achieve the strain-balance condition. The GaN barrier thickness was fixed at 80 Å. The horizontal dotted lines in each sub-figure represent the region of bandgaps for each QW structure that is of interest for various multi-junction solar cell designs as discussed in the text.

and ΔE is given as follows [56]:

$$\Delta E = -2a \left(\frac{C_{11} - C_{12}}{C_{11}} \right) \varepsilon. \quad (2)$$

The second effect due to strain is the splitting of the heavy hole (hh) and light hole (lh) degeneracy. For a compressive material, the heavy hole will move to a higher energy, while for a tensile material the light hole will be at a higher energy. The magnitudes of energy splitting for heavy holes (ΔE_{hh}) and light holes (ΔE_{lh}) depend upon the shear deformation potential, "b" [56]

$$\Delta E_{hh} = b \left(\frac{C_{11} + 2C_{12}}{C_{11}} \right) \varepsilon$$

$$\Delta E_{lh} = -b \left(\frac{C_{11} + 2C_{12}}{C_{11}} \right) \varepsilon. \quad (3)$$

The elastic stiffness's, hydrostatic-pressure, and shear deformation potential values used in the strain effects calculations are obtained from Adachi [54]. The last term in (1), ΔE_G^{QCSE}, represents the well thickness-dependent shift in the effective band gap due to the quantum-confined stark effect (QCSE) [52], [53].

$$\Delta E_G^{QCSE} = \left(\frac{15 - \pi^2}{24\pi^2} \right) \left(\frac{m_e^* L_{eff,CB}^4 + m_h^* L_{eff,VB}^4}{\hbar^2} \right) qF^2 \quad (4)$$

where m^* is the effective mass, q is the elemental charge, $\bar{h}$ is the reduced Planck constant, $L_{eff,CB}$ and $L_{eff,VB}$ are the effective QW width in the conduction and valence band [57], and F is the induced electric field due to spontaneous and piezoelectric polarization.

The $E_{G,Eff}$ of strain-balanced InGaAs/GaAsP and strain-balanced InGaAsP/InGaP was calculated using (1). The $E_{G,Eff}$ of strained InGaN/GaN was calculated using a physics-based software to solve Schrodinger–Poisson for the QW bound state energy. The effective bandgap of strain-balanced $In_xGa_{1-x}As/GaAs_{0.35}P_{0.65}$, strain-balanced

$In_xGa_{1-x}As_{0.10}P_{0.90}/In_{0.40}Ga_{0.60}P$, and strained In_xGa_{1-x} N/GaN versus well thickness (t_w) for various indium compositions, x, are shown in Fig. 3. The barrier thickness (t_b) of $GaAs_{0.35}P_{0.65}$ and $In_{0.40}Ga_{0.60}P$ were adjusted to achieve the strain-balance condition. The GaN barrier thickness was fixed at 80 Å. The horizontal dotted lines in each sub-figure represent the region of bandgaps for each QW structure that is of interest for various multi-junction solar cell designs. For example, a 1.2 eV InGaAs/GaAsP QW can be used as the middle junction in triple-junction devices (1.8/1.2/0.7 eV) [25], [28], [32], [34], [39]. Also, InGaAs/GaAsP with a bandgap of 1.1 eV is a potential candidate for the bottom cell material in dual-junction (1.7/1.1 eV) solar cell [58]. Also, InGaAs/GaAsP has been proposed as a 1.15 eV subcell in quad-junction devices [37]. Similarly, InGaAsP/InGaP QW solar cell has been proposed as a 1.6–1.7 eV subcell in next-generation five- and six-junction devices [41], [42] and as the top cell in triple-junction devices (1.75/1.2/0.7 eV). In addition, InGaAsP/InGaP with a bandgap of 1.6–1.8 eV is also a potential candidate as an III–V top cell material in III–V/Si dual-junction [58]. Also, developing InGaN with bandgap higher than 2 eV is important for multiple-junction junction devices [13], [44]–[47], [59].

As shown in Fig. 3, as the QW thickness increases, QSEs are being reduced thus the $n = 1$ quantum state moves downward resulting in a red-shift in the effective bandgap. The effective bandgap reduces monotonically by increasing the indium composition. The field, F, is in the MV/cm range for the InGaN/GaN structure and is in kV/cm range in the GaAs-based and InGaP-based structures. Thus, QCSE plays a dominant role in controlling the emission and absorption processes in the GaN-based QW structures and can be neglected in the GaAs-based QW structures. The increase of the indium percentage in InGaN increases F and QCSE and results in a red-shift in the bandgap. It is noted that there is more than one design in each of these structures that can theoretically realize the target bandgap in each of these structures. For example, a 1.2 eV InGaAs/GaAsP QW solar cell can be achieved using an $In_{0.25}Ga_{0.75}As$ QW of
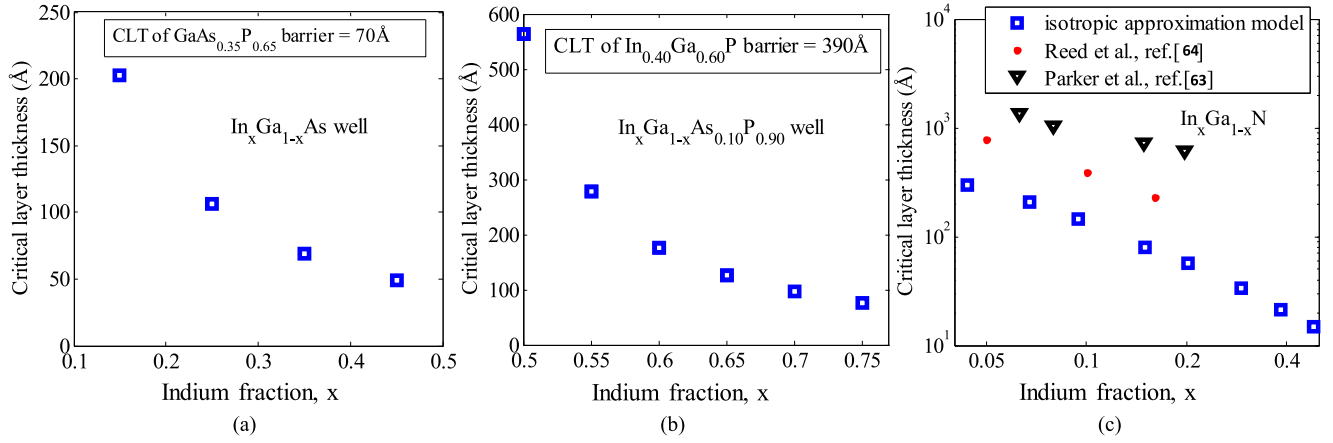
Fig. 4.   Critical layer thickness versus the indium fraction, x, for (a) $In_xGa_{1-x}As$ well, (b) $In_xGa_{1-x}AsP$ well, and (c) $In_xGa_{1-x}N$ well.

thickness 80 Å or an $In_{0.45}Ga_{0.55}As$ QW of thickness 30 Å. The choice of the well/barrier thicknesses and compositions is a design factor that is challenged by other factors such as CLT, strain balance, material quality, and carrier transport constraints as will be discussed in the next few sections.

B. Critical Layer Thickness Constraints

InGaAs(P) and InGaN QWs can be grown compressively strained to GaAs substrates and GaN templates on sapphire substrates, respectively, provided that the film thickness remains less than the CLT. The CLT is a thickness below which a material can be grown fully strained without the formation of misfit dislocations [16], [60], [61]. The CLT is a function of strain, ε, caused by lattice mismatch between the film and substrate, where $\varepsilon = \frac{a_{\text{film}} - a_{\text{sub.}}}{a_{\text{sub.}}}$; a_{film} and $a_{\text{sub.}}$ are the lattice constants of film and substrate, respectively. A larger lattice mismatch yields a larger strain build up and results in a lower CLT. The CLT of InGaAs and InGaAsP QWs are calculated using Matthews and Blakeslee [60], which has a good agreement with experimental results for III–V semiconductors, see Fig. 4(a) and (b). The CLT of InGaN was modeled using the isotropic approximation core energy method [62] and experimental values by Parker *et al.* and Reed *et al.* are also used [63], [64], as shown in Fig. 4(c). As shown in Fig. 4, the CLT depends critically on the value of indium, x, for the three QW structures. For example, the CLT of $In_xGa_{1-x}As$ films with $x = 0.15$, 0.25, and 0.35 are 202, 106, and 70 Å, respectively, as shown in Fig. 4(a). The CLT of $InGaAs_{0.10}P_{0.90}$ films is reduced from 563 Å for an indium fraction of 0.5 to 126 Å for an indium fraction of 0.65. Similarly, the CLT of InGaN reduces significantly by increasing the indium fraction (x), as shown in Fig. 4(c). The spread in the data for the CLT of InGaN is due to whether it is estimated for a bulk InGaN layer or for InGaN as part of an InGaN/GaN QW structure.

Unfortunately, the amount of indium needed to achieve the optimum bandgap for the InGaAs(P) and InGaN would create a mismatch that limits CLT to a few hundred Angstroms or less. This indicates that the individual layers thickness in the QW structure should be grown less than the CLT to avoid the onset of the dislocations. Unfortunately, this thin well thickness

will not provide enough optical absorption to create an effective QW subcell in multi-junction solar cells. Hence, researchers have focused on growing a high number of period QW devices with individual layers thicknesses less than the CLT in order to increase the total thickness of absorbing wells without sacrificing the CLT limitations.

C. Strain Balance Design and Criteria

Even if the individual layers in the periodic QW structure are grown less than the CLT, the whole structure may relax if the strain-balance condition was not fully realized. If the strain-balance condition was not met, there will be a net accumulation of compressive or tensile stress in whole multiple QW structure that can lead to lattice mismatch with the substrate. The excess of compressive or tensile stress will result in the relaxation of strained layers and will form dislocation defects. This is particularly observable during the growth of a high number of periods (for instance, higher than 50) which is required to enhance the external quantum efficiency of the QW structures. For instance, strained InGaAs/GaAs QW solar cell has a limited external quantum efficiency of less than 20% beyond the band-edge of GaAs due to a limited number of QWs that can be included [65]. Increasing the number of strained QWs can increase the dark current, and degrades FF and η. This is also a challenge hindering the development of high-performance InGaN/GaN because the net strain, mainly in the InGaN layers, will always be compressive and limited number of periods can be grown [44], [47], [48].

There are four parameters that can be controlled during the QW growth to strain-balance the structure
1) t_w;
2) t_b;
3) lattice constant of well (a_w);
4) lattice constant of barrier (a_b).

There are several models to strain-balance these QW structures. One simple model is the average-lattice method, which arises from the thickness average of compressive and tensile parameters [66]

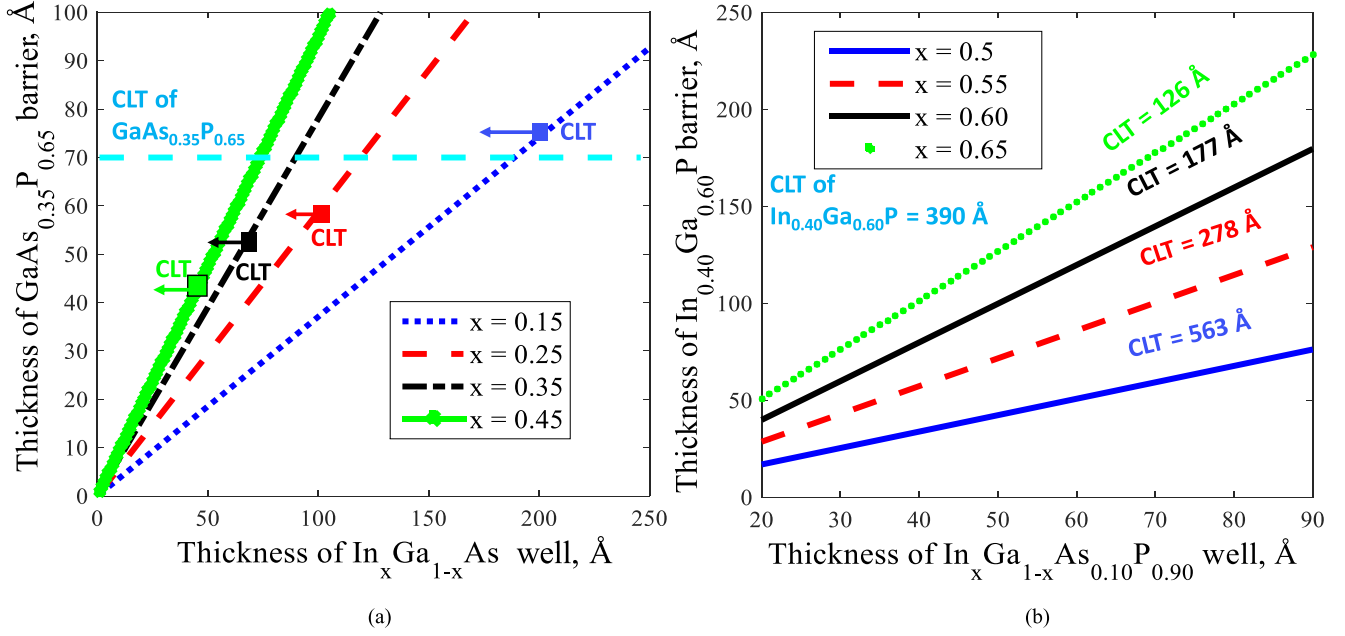$$(a_w - a_{\text{temp.}})t_w = (a_b - a_{\text{temp.}})t_b \qquad (5)$$

Fig. 5. Thickness of wells and barriers as estimated by zero-stress balance model to strain-balance the following two structures to GaAs substrates. (a) InGaAs/GaAs$_{0.35}$P$_{0.65}$ with various indium fraction, x, in InGaAs well. (b) InGaAs$_{0.10}$P$_{0.90}$/In$_{0.40}$Ga$_{0.60}$P with various indium fraction, x, in the InGaAsP well. The CLT of each well composition is added to the figure. The CLT of the barrier and each well in Figure b is outside the range of the presented y- and x-axes scale.

where $a_{\text{temp.}}$ is the lattice constant of the underlying template (GaAs or GaN). Equation (5) assumes identical elastic properties for the well and barrier which can be inaccurate. A zero-stress balance model, by Ekins-Daukes *et al.*, takes into account the differences in elastic properties of the wells and barriers [66]. The model relies on minimizing the average in-plane stress due to biaxial strain in the QWs/barriers, and thus gives better estimates for thicknesses that realize the strain-balance condition more than the average-lattice method. The condition to achieve a stress-balance, the QWs is as follows [66]:

$$A_w t_w \varepsilon_w a_b + A_b t_b \varepsilon_b a_w = 0 \qquad (6)$$

$$a_{\text{temp.}} = \frac{A_w t_w a_w a_b^2 + A_b t_b a_b a_w^2}{A_w t_w a_b^2 + A_b t_b a_w^2} \qquad (7)$$

where ϵ_w and ϵ_b are the strain in wells and barriers, respectively. A_w and A_b are the stiffness parameters for wells and barriers, respectively, which are calculated as follows:

$$A = C_{11} + C_{12} - \frac{2C_{12}^2}{C_{11}}. \qquad (8)$$

The thicknesses of wells and barriers obtained from the zero-stress model to strain-balance In$_x$Ga$_{1-x}$As/GaAs$_{1-y}$P$_y$ and In$_x$Ga$_{1-x}$As$_{1-z}$P$_z$/In$_y$Ga$_{1-y}$P QW structures are shown in Fig. 5. There can be no similar graph for the strained In-GaN/GaN because the net strain in the whole structure will be always compressive. The effects of indium composition in InGaAs well and InGaAsP well are studied in Fig. 5(a) and (b), respectively. The range of the indium compositions of In-GaAsP is higher than 49% as mentioned earlier. In Fig. 5, the compositions of GaAsP and InGaP barriers are fixed and the arsenic in InGaAsP well is set to 10%. The CLT of each well

composition is also added to the figure. We first notice that as the well thickness increases, the compressive stress increases and the required barrier thickness to strain-balance the structure will also increase. For instance, In$_{0.15}$Ga$_{0.85}$As with well thickness of 25 and 100 Å can be strain-balanced by a GaAs$_{0.35}$P$_{0.65}$ barrier with t_b of 10 and 40 Å, respectively. It is also noted that for a fixed barrier thickness and composition, InGaAs(P) with wells having higher indium percentage will be thinner than those with lower indium content as shown in Fig. 5. These curves can be used as a design guideline to estimate the thicknesses needed to achieve nearly strain-free QW structures.

D. Carrier Transport

QW solar cells are p-i-n structures, where the QWs are located in the intrinsic (i) layer. Carriers, optically generated in the QWs, are either collected by the built-in field that exists in the QW region or lost due to carrier recombination. There are two QW approaches to collect carriers by drift: 1) use of thin wells, and carriers are transported by electric field via thermionic emission as shown in Fig. 6(a), and 2) use of thin barriers, and carriers are transported by electric field via tunneling as shown in Fig. 6(b). Carrier transport by an electric field, via thermionic emission, requires growing thin wells ($\sim$50 Å) with low effective barrier height ($\sim$ few kT, where k is Boltzmann's constant and T is the temperature). The realization of carrier transport by tunneling requires the use of thin barriers ($\sim$20–40 Å) and the reduction of effective barrier heights. The escape lifetime ($\tau_{esc.}$) of a carrier from a QW is determined by the thermionic emission and tunneling lifetimes as follows [67]:

$$\frac{1}{\tau_{esc.}} = \frac{1}{\tau_{\text{tun.}}} + \frac{1}{\tau_{\text{therm.}}}, \qquad (9)$$
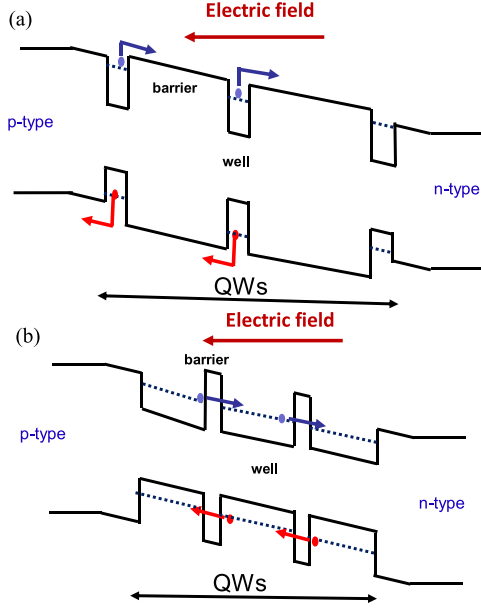
Fig. 6. Band diagram of quantum well solar cells with two different designs. (a) Structure with thin wells and low effective barrier height to promote thermionic emission. (b) Structure with thin barriers to allow carrier tunneling. In both scenarios, the carriers are swept across the depletion region by the electric field.

where $\tau_{\text{tun.}}$ and $\tau_{\text{therm.}}$ are tunneling and thermionic-emission lifetimes, respectively. $\tau_{\text{tun.}}$ and $\tau_{\text{therm.}}$ can be expressed as follows [67]–[69]:

$$\frac{1}{\tau_{\text{tun.}}} = \frac{n\pi\hbar}{2t_w^2 m_w^*} e^{-\frac{2}{\hbar}\int_0^{t_b}\sqrt{2m_b^*(E_b - E(z)z)}dz} \quad (10)$$

$$\frac{1}{\tau_{\text{therm.}}} = \frac{1}{t_w}\sqrt{\frac{kT}{2\pi m_w^*}} e^{-\frac{E_b}{kT}} \quad (11)$$

where m_w^* and m_b^* are the effective masses at the well and the barrier, respectively. E_b is the effective barrier height from the ground state ($n = 1$), and $E(z)$ is the electric field. The escape probability of minority carriers from a single QW, P_i, can be calculated as follows [67]:

$$P_i = \frac{\frac{1}{\tau_{\text{esc.}}}}{\frac{1}{\tau_{\text{esc.}}} + \frac{1}{\tau_{\text{rec.}}}} \quad (12)$$

where $\tau_{\text{rec.}}$ is the recombination lifetime. Thus, the probability of carrier collection is high, for QWs with long carrier lifetime and short escape lifetime, i.e., $\tau_{\text{esc.}} \ll \tau_{\text{rec.}}$. This does impose restrictions on material quality. If we assume that the escape probabilities from all the QWs are the same, the total escape probability can be expressed as follows:

$$P_{\text{tot.}} = P_i^N \quad (13)$$

where N is the number of QWs in the intrinsic region. For example, if the escape probability (P_i) across a single QW is 0.98, the total escape probability ($P_{\text{tot.}}$) across 20 QWs, is $0.98^{20} = 0.67$, which is not high enough to guarantee efficient carrier collection by drift. Hence, the thickness of well and barrier, as well as the effective barrier height should be tuned to maximize

the carrier escape probability without sacrificing the material quality. Equation (13) assumes all carriers generated in the QW and neutral regions will traverse N QWs. However, each carrier traverses a different number of wells, depending on the position where the carrier was generated. It should also be mentioned that (13) assumes a simplistic case of 100% capture, which might not be very accurate for a high background doping in the QW region as will be discussed in Section VI.

For $In_{0.11}Ga_{0.89}As$ (93 Å)/$GaAs_{0.93}P_{0.07}$ (160 Å), the thermionic-emission lifetimes for electrons, calculated using (11) for the first quantum state is ~7 ns, which is more than 1000 times higher than tunneling lifetime (1.68 ps), thus indicating that carriers are transported by drift using thermionic emission. If the QWs are fully strain-balanced with high material quality, the recombination lifetime, $\tau_{\text{rec.}}$, will be much longer than $\tau_{\text{therm.}}$ and this will lead to a 100% escape probability for the carriers swept by drift as indicated by (12). If we assume a structure that has a thin barrier thickness such as $In_{0.18}Ga_{0.82}As$ (125 Å)/$GaAs_{0.36}P_{0.64}$ (40 Å), the tunneling and thermionic-emission escape lifetimes, $\tau_{\text{tun.}}$ and $\tau_{\text{therm.}}$, for electrons are 0.89 ns and 1.84 μs, respectively. The shorter tunneling escape time indicates that tunneling is dominating the transport. If a recombination time, $\tau_{\text{rec.}}$, of 50 ns is assumed, the tunneling escape probability across a single QW and 100 QWs will be 0.984 and $0.984^{100} = 0.1686$ as calculated using (12) and (13), respectively. The escape probability across the 100 QWs is not sufficiently high for efficient carrier collection. If the $GaAs_{0.36}P_{0.64}$ barrier thickness is reduced from 40 to 20Å, $\tau_{\text{tun.}}$ will be reduced from 0.89 ns to 4.1276 ps, thus increasing the escape probability across the 100 QWs from 0.1686 to 0.9918. This indicates that the use of thin-barriers is essential for tunneling to take place efficiently. The same discussion is also valid for the holes. In the next section, different QW material systems are studied and the effects of different QW designs on carrier transport and collection are analyzed.

IV. TUNING SUBCELLS ABSORPTION THRESHOLD USING QUANTUM WELLS

In this section, three QW solar cell structures that have been widely researched are discussed. For each QW structure, we analyze the state-of-the-art solar cell results and discuss the major challenges and advancements in the field.

A. Strain-Balanced InGaAs/GaAsP Quantum Wells to Achieve a 1.1–1.3 eV Subcell

InGaAs/GaAsP is grown in the unintentionally doped i layer of GaAs n-i-p (or p-i-n) solar cells as shown in Fig. 1(a). The emitter and base are GaAs doped typically with silicon (or selenium) and zinc (or carbon), respectively. There are several potential applications of this QW structure in multi-junction solar cells. First, InGaAs/GaAsP has been widely used in triple-junction devices (1.8/1.2/0.7 eV) to tune the bandgap of GaAs solar cells to 1.2 eV to increase the short-circuit current (J_{sc}) and alleviate the current mismatch between the top and middle cells [25], [28], [32], [34], [39]. In addition, InGaAs/GaAsP with a bandgap of 1.1 eV is a potential candidate for the
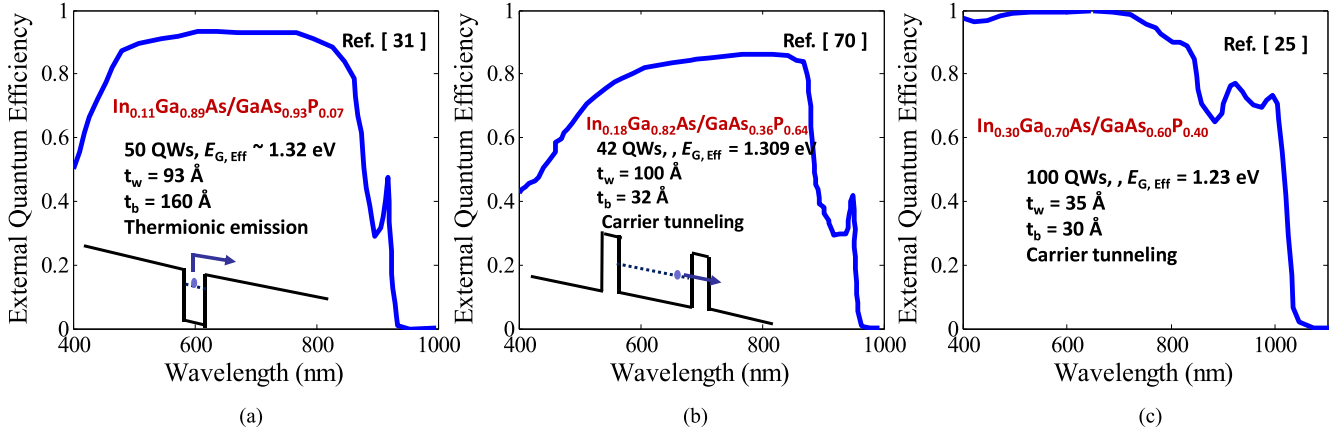
Fig. 7. External quantum efficiency of multiple InGaAs/GaAsP quantum well solar cells designs. (a) Structure with thin wells and low effective barrier height to promote the carrier transport by electric field via thermionic emission, by Adams *et al.* [31]. (b) Structure with thin barriers to allow carrier tunneling, by Bradshaw *et al.* [32], [70]. (c) High-performance structure with peak excitonic values exceeding 70%, by Fujii *et al.* [25]. More details about these structures such as the presence of window, back surface field or antireflection coatings are discussed in the references.

TABLE I
TUNNELING (P_{tun}) AND THERMIONIC-EMISSION (P_{therm}) ESCAPE PROBABILITIES FOR ELECTRONS AND HEAVY
HOLE STATES FOR DIFFERENT INGAAS/GAASP QW DESIGNS

	$P_{tun.}$		P_{therm}		Carrier transport
	e	hh	e	hh	
$In_{0.11}Ga_{0.89}As$ (93 Å)/ $GaAs_{0.93}P_{0.07}$ (160 Å), 50-period [31]	0	0	0.9983	0.9983	By drift via thermionic emission
$In_{0.18}Ga_{0.82}As$ (100 Å)/ $GaAs_{0.36}P_{0.64}$ (32 Å), 42-period [32, 70]	0.9431	0.94	0.1447	0	By drift via carrier tunneling
$In_{0.30}Ga_{0.70}As$(35 Å)/ $GaAs_{0.60}P_{0.40}$(30 Å), 100-period [25]	1	0.9584	0.5672	0	By drift via carrier tunneling

bottom cell material in dual-junction (1.7/1.1 eV) solar cell, with a prospective one-sun AM1.5G efficiency of 36%–38% [58]. Recent efforts by NCSU/Spectrolab have shown the successful integration of $In_{0.49}Ga_{0.51}P$ (1.9 eV) top cell with GaAs bottom cell that incorporates InGaAs/GaAsP QWs [39]. Also, InGaAs/GaAsP has been proposed as a 1.15 eV subcell in quad-junction devices with a prospective efficiency of 50% [37].

Researchers have developed InGaAs/GaAsP QWSCs based on the two carrier transport mechanisms discussed in Section III-D and Fig. 6. In order to realize the carrier transport by electric field via thermionic emission in InGaAs/GaAsP, the high-bandgap strain-compensating barrier, GaAsP, must have a composition that yields lattice constant and bandgap close to GaAs substrate such that the effective barrier height for electrons and holes will be sufficiently low to surmount, as shown in the band diagram of Fig. 6(a). The external quantum efficiency (EQE) of 50-period $In_{0.11}Ga_{0.89}As$ ($t_w = 93$ Å)/$GaAs_{0.93}P_{0.07}$ ($t_b = 160$ Å), by Adams *et al.* [31], is shown in Fig. 7(a). The conduction band diagram for that structure is also shown in the inset of the same figure. It is noted that the phosphorus and indium compositions in the GaAsP barrier and InGaAs layers are only 7% and 11%, which will lead to a tensile and compressive strain of –0.25% and 0.8%, respectively. For wavelengths (λ) shorter than the GaAs band-edge (885 nm), absorption occurs in the GaAs:p emitter and GaAs:n base and the high EQE

values indicates efficient light absorption and carrier collection. For λ's longer than the GaAs band-edge, absorption occurs in the InGaAs/GaAsP QWs, and the inclusion of QWs in the intrinsic region has extended the absorption threshold to ~932 nm. The high EQE values beyond GaAs-band-edge (hereafter, sub-bandgap EQE) that are exceeding 40% at 920 nm indicates that the electric field sweeps away all the carriers efficiently across the depletion region. We calculated the escape probability for electrons and holes for that structure using (9)–(13), and the values are summarized in Table I. The effective barrier heights for electrons and holes are 77 and 80 meV, respectively, which yields to a unity thermionic probability (P_{therm}) across a single QW and across the 50 QWs. The thick $GaAs_{0.93}P_{0.07}$ barrier (160 Å) leads to zero tunneling probability (P_{tun}) for both electrons and holes, see Table I. Even though that the research presents efficient light absorption and carrier collection, the percentage of the total absorbing InGaAs well (0.465 μm) represents only 37% of the total period thickness (1.26 μm). This is attributed to the use of the low-phosphorus composition in the GaAsP, which will limit the increase of the absorbing InGaAs well thickness to maintain the strain-balance condition. If the InGaAs well thickness is further increased, the strain-balance condition will be violated resulting in the presence of defects, which will degrade the η. One possible approach to address this issue is to increase the number of QWs to
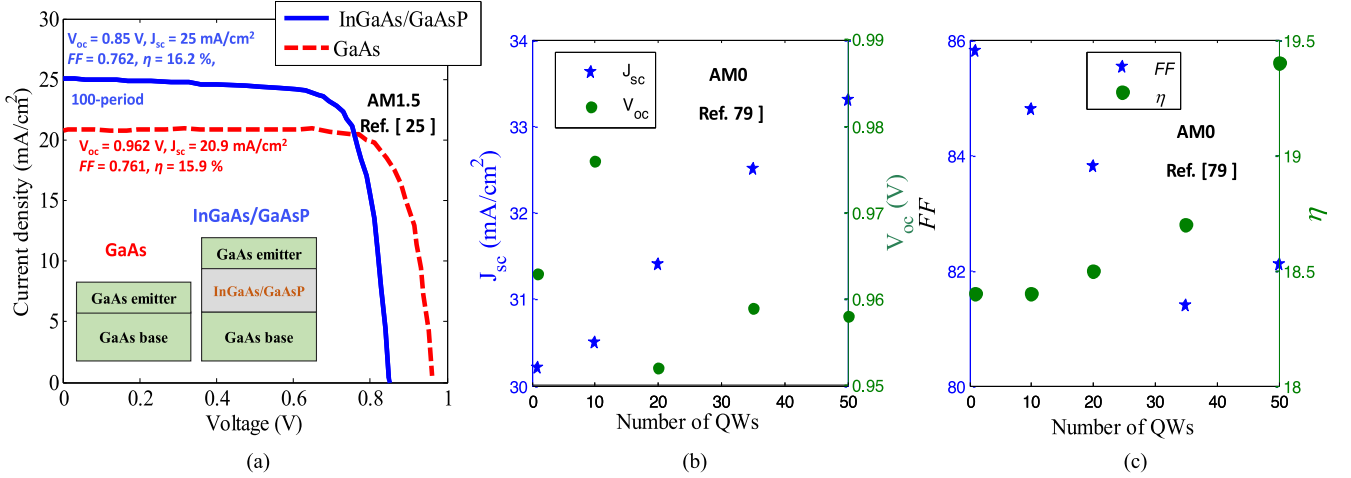
Fig. 8. (a) AM1.5 current–voltage characteristics of InGaAs/GaAsP QW and GaAs standard solar cells, with the inset showing a schematic of the two structures, by Fujii *et al.* [25]. The effect of the number of QWs in the intrinsic region on one-sun AM0 current–voltage characteristics. (b) J_{sc} (mA/cm^2) and V_{oc} (Volts) and (c) FF and η; study by Bushnell *et al.* [79].

enhance the sub-bandgap EQE. However, increasing the number of QWs is typically accompanied by limitations associated with epitaxial growth challenges such as the strain-balance and CLT issues as discussed in Section III, as well as the difficulty of obtaining a uniform electric field distribution across the QW region as will be discussed later in Section VI.

In order to address that limitation, another QW approach was proposed by NCSU that relies on using thicker absorbing wells and thin barriers through the use of high phosphorus in the GaAsP barriers [32], [71], [72]. The high phosphorus composition creates a larger compensating strain, therefore allowing the barriers to be thin enough that carriers are swept by drift through tunneling across the barriers [32]. This removes two limitations that exist in the structure, as shown in Fig. 7(a), that has low phosphorus GaAsP layers. First, the absorbing InGaAs layers of this approach form the majority of the QW region which can lead to enhancing the sub-bandgap EQE. Second, the indium composition of the InGaAs is not limited by the requirement that effective barrier height should be sufficiently low for the carriers to surmount. For 100-period $In_{0.14}Ga_{0.86}As$ ($t_w = 115$ Å) and $GaAs_{0.24}P_{0.76}$ ($t_b = 27$ Å) QWs, the thickness of the non-absorbing $GaAs_{0.24}P_{0.76}$ barriers leads to only ~ 0.27 μm total barrier thickness. Thus, the i layer will primarily consist of $In_{0.14}Ga_{0.86}As$ optical absorbing films, ~ 1.1 μm, which is much thicker than the corresponding InGaAs thickness in the structure that relies on the carrier transport by drift via thermionic emission. This will correspond to enhancement in the sub-bandgap EQE and will enhance the gain in J_{sc} if compared with that of a GaAs cell that does not include QWs. Fig. 7(b) shows the EQE of 42-period $In_{0.18}Ga_{0.82}As$ ($t_w = 100$ Å)/$GaAs_{0.36}P_{0.64}$ ($t_b = 32$ Å), by Bradshaw *et al.* [32], [70]. The EQE values in Fig. 7(b) indicate efficient light absorption and carrier collection in both the bulk region and the QW region. The values for the probabilities for tunneling and thermionic emission, $P_{tun,}$ and $P_{therm.}$ are summarized in Table I. The thin $GaAs_{0.36}P_{0.64}$ barriers (30 Å) allow for the carriers to tunnel efficiently across both single well and the

42-QWs. The P_{therm} across the QWs are less than 15% due to the high effective barrier height (0.413 eV for electrons and 0.2336 eV for holes).

There are several challenges with the growth of the InGaAs/GaAsP QW structure. First, it is challenging in terms of crystal growth to achieve such high phosphorus composition in GaAsP. This is because arsenic incorporates more efficiently than phosphorus when both arsine (AsH_3) and phosphine (PH_3) are present possibly due to the differences in their sticking coefficients and pyrolysis rates [73]–[75]. The success behind growing 70% phosphorus GaAsP was realized by research groups that used tertiarybutylphosphine (TBP) and tertiarybutyl-arsine (TBA), with a [TBP]/([TBP]+[TBA]) flow ratio higher than 80% [25], [76].

The second challenge is related to the group V switching at InGaAs/GaAsP interfaces, which result in graded (non-abrupt) interfaces [77]. This leads to the formation of an unintentional quaternary InGaAsP alloy. This difficulty arises due to phosphorus and arsenic atoms intermixing as well as phosphorus carry-over. In order to improve (In,Ga)As/Ga(As,P) interface quality, a GaAs interfacial was introduced, by Samberg *et al.*, at both the InGaAs/GaAsP and GaAsP/InGaAs interfaces [77]. The GaAs transition layers have proved to prevent the phosphorus carryover between the barrier and well structures resulting in improvements in the electrical and material characteristics [25], [32], [77], [78].

A 100-period $In_{0.30}Ga_{0.70}As$ (35 Å)/GaAs(27Å)/$GaAs_{0.60}P_{0.40}$(30 Å) with an effective bandgap of 1.23 eV has been demonstrated, by Fujii *et al.* [25], as shown in Fig. 7(c). The EQE values exceed 80% beyond band-edge of GaAs, thus indicating efficient light absorption and carrier collection, as well as excellent control over growth conditions. The carriers are swept across the depletion through tunneling as indicated by the $P_{tun.}$ and P_{therm} values in Table I. The one-sun AM1.5 current density–voltage curve measured for the 100-period device, as well as, a GaAs device that does not include QWs, is shown in Fig. 8(a) [25]. A schematic of the two structures is also

depicted in the inset of Fig. 8(a). The J_{sc}, V_{oc}, FF, and η of the 100-period $In_{0.30}Ga_{0.70}As/GaAs_{0.60}P_{0.40}$ QW device were 25 mA/cm^2, 0.85 V, 76.2%, and 16.2%, respectively. The corresponding J_{sc}, V_{oc}, FF, and η values of GaAs standard device were 20.9 mA/cm^2, 0.962 V, 0.761, and 15.9%, respectively. The reported J_{sc} for the QW device is ∼20% higher than the GaAs device [25]. The reason for J_{sc} enhancement is due to the sub-bandgap absorption by the QWs as shown in the EQE of Fig. 7(c). The V_{oc} of QW device is 115 mV lower than the GaAs device due to extending the bandgap to 1.23 eV.

The η of the QW device is higher than the GaAs (w/o QWs) device due to the large J_{sc} boost. Current–voltage characteristics showing J_{sc} and η improvements due to the addition of the QWs were also reported by the NCSU and Imperial College groups [32], [34]. More details about the structures discussed in Fig. 7, such as the presence of window, back surface field, or antireflection coatings, are discussed in the references.

The effect of the number of periods on strain-balanced $In_{0.10}Ga_{0.90}As$ ($t_w = 80$ Å)/$GaAs_{0.92}P_{0.08}$ (t_b=186 Å) device performance is depicted in Fig. 8(b) and (c), using the tabulated data reported by Bushnell et al. [79]. It is worth pointing out that the carriers in this QW structure will be swept by drift through thermionic emission due to the use of low phosphorus barrier ($GaAs_{0.92}P_{0.08}$). There are two competing effects occurring with the increase in the number of QWs. First, the increase of the QW number enhances the J_{sc} due to increasing the total thickness of absorbing layers, see Fig. 8(b). Second, a larger number of QWs increases the dark current due to an increase in the depletion region thickness and number of interfaces, and thus increases the Shockley Read Hall (SRH) recombination rate. The increase or decrease of V_{oc}, with the number of QWs, depends on the last two effects, and it typically does not vary significantly with the number of period change, as shown in Fig. 8(b). Increasing the number of QWs from 1 to 50 has reduced the FF from 85.8% to 82.1%. This can be attributed to an expected increase in the total stress across the QW, and improving the FF higher than 85% requires more enhancement of interfaces quality and excellent stress management to reduce the stress across the QW region. High-performance QW devices have a boost in J_{sc} that compensate both the V_{oc} and FF deterioration, thus resulting in an increase in efficiency if compared with standard GaAs devices, as shown in Fig. 8(a) and (c).

B. Strain-Balanced and Lattice-Matched InGaAsP/InGaP Quantum Wells to Achieve a 1.6–1.8 eV Subcell

InGaAsP/InGaP is grown in the unintentionally doped i layer of $In_{0.49}Ga_{0.51}P$ n-i-p (or p-i-n) solar cells for both the strain-balanced structure shown in Fig. 1(b3) and the lattice-matched structure shown in Fig. 1(b2). For n-i-p structure, the emitter and base are $In_{0.49}Ga_{0.51}P$ lattice-matched to GaAs substrates, doped typically with silicon (or selenium) and zinc, respectively. There are several potential applications of this QW structure in multi-junction solar cells. First, extending the absorption threshold of $In_{0.49}Ga_{0.51}P$ (1.85 eV) solar cells to the 1.6–1.75 eV range, makes it promising for potential use as the second highest energy subcell in next-generation five- and six-

junction devices [41], [42], [80]. Also, InGaAsP/InGaP is a prospective top cell in triple-junction devices (1.75/1.2/0.7 eV) to alleviate the current mismatch between top and middle cells [35]. In addition, InGaAsP/InGaP with a bandgap of 1.6–1.8 eV is also a potential candidate as a III–V top cell material in III–V/Si two-junction cells, with a prospective one-sun AM1.5G efficiency of 36%–38% [58]. Quaternary InGaAsP alloys are promising for such applications and have attained many interests recently for the development of optoelectronic devices such as solar cells [81] lasers [82]–[84], and aluminum-free near-infrared LEDs [85], [86]. However, due to the presence of the miscibility gap, limited composition range was successfully synthesized [87] and bandgap tunability might be limited.

Researchers have developed InGaAsP/InGaP QWSCs based on the two carrier transport mechanisms discussed in Section III-D and Fig. 6. The first approach, developed by Sayed et al. [42], [43], is the strain-balanced $In_xGa_{1-x}As_{1-z}P_z$/$In_yGa_{1-y}P$ QWs grown in the i region of $In_{0.49}Ga_{0.51}P$ p-i-n, as shown in Fig. 1(b3). The strain-balanced $In_xGa_{1-x}As_{1-z}P_z$/$In_yGa_{1-y}P$ QW structure has a wide tunable bandgap (1.5–1.8 eV) thus making it promising for several multi-junction devices, where $0.50 < x < 0.75$, $0.35 < y < 0.45$, and $0.9 < z < 0.98$. InGaAsP is grown with indium composition of higher than 49%, to tune the bandgap of $In_{0.49}Ga_{0.51}$P-based cells (1.85 eV) to the 1.6–1.8 eV range. In the strain-balanced InGaAsP/InGaP QW approach, the highly strained low-bandgap layer, InGaAsP well, has a thin thickness (30–70 Å) and the InGaP barrier has a lattice constant close to that of the GaAs substrate to reduce the effective barrier height for electrons and holes to enable the sweep of the carriers by drift through thermionic emission. The EQE of strain-balanced 30-period $In_{0.70}Ga_{0.30}As_{0.05}P_{0.95}$ ($t_w = 45$ Å)/$In_{0.40}Ga_{0.60}P$ ($t_b = 140$ Å) is depicted in Fig. 9(a); the inset shows the conduction band-diagram for such structure [42]. For λ's longer than the $In_{0.49}Ga_{0.51}P$ (680 nm), absorption occurs only in the InGaAsP QW. The P_{tun} and P_{therm} values were calculated for this structure using (9)–(13), and the values are summarized in Table II. The thick $In_{0.40}Ga_{0.60}P$ barrier (140 Å) inhibits the carriers to tunnel across it thus resulting in zero tunneling probability. The effective barriers for electrons and holes are 0.1622 and 0.2745 eV, respectively, which lead to 1 and 0.5 thermionic emission probabilities for electrons and holes, respectively.

The second generation of the InGaAsP/InGaP QW structure is grown lattice matched to the GaAs-substrate, in the i region of $In_{0.49}Ga_{0.51}P$ n-i-p shown in Fig. 1(b2). The growth of QWs and barriers lattice-matched removes the CLT constraints because the strain-balanced condition is automatically achieved. Thus, a higher number of periods can be grown for the lattice-matched structure than the strain-balanced structure, because it is easier to manage stress during growth. In addition, the lattice-matched structure offers a great design flexibility in choosing the various layers thicknesses and thus the carrier transport mechanism. Two QW designs are proposed in the literature. The first lattice-matched design, by Lee et al. [35], is based on thick $In_{0.49}Ga_{0.51}P$ barriers, where the carriers are being transported by the electric field via thermionic emission. The second design, by Sayed et al. [41], is
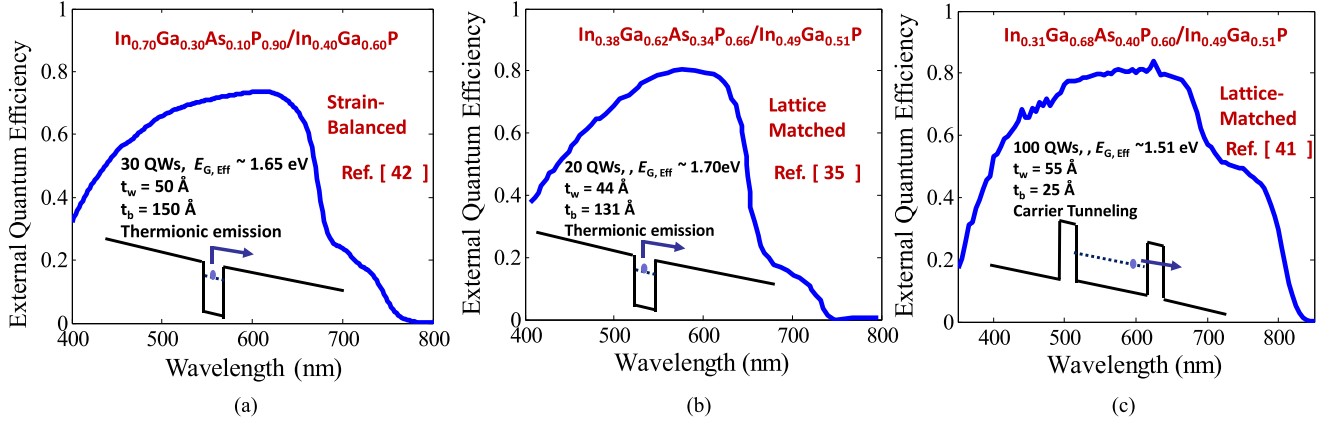
Fig. 9. External quantum efficiency of multiple InGaAsP/GaAsP quantum well solar cells designs. (a) Strain-balanced structure with thin wells and low effective barrier height to promote the drift of the carriers through thermionic emission, by Sayed *et al*. [42]. (b) Lattice-matched structure with thin wells and low effective barrier height to promote the drift of the carriers through thermionic emission, by Lee *et al*. [35]. (c) High-performance 100-period structure with peak excitonic values exceeding 50%, by Sayed *et a*l. [41]. More details about these structures such as the presence of window, back surface field or antireflection coatings are discussed in the references.

TABLE II
TUNNELING (P_{tun}) AND THERMIONIC-EMISSION (P_{therm}) ESCAPE PROBABILITIES FOR ELECTRONS AND HEAVY HOLE STATES FOR
DIFFERENT INGAASP/INGAP QW DESIGNS

	$P_{tun.}$		P_{therm}		Carrier transport
	e	hh	e	hh	
Strain-balanced $In_{0.70}Ga_{0.30}As_{0.05}P_{0.95}$ (45 Å)/ $In_{0.40}Ga_{0.60}P$ (140 Å), 30-period [42]	0.0	0.0	1	0.5824	By drift via thermionic emission
Lattice-matched $In_{0.38}Ga_{0.62}As_{0.34}P_{0.66}$ (t_w= 44 Å)/ $In_{0.49}Ga_{0.51}P$ (t_b= 133 Å), 20-period [35]	0.9980	0.0	1	0.86	By drift via thermionic emission
Lattice-matched $In_{0.32}Ga_{0.68}As_{0.55}P_{0.45}$ (t_w= 55 Å)/ $In_{0.49}Ga_{0.60}P$ (t_b= 25 Å), 100-period [41]	0.9998	0.9846	0.9991	0.0	By drift via carrier tunneling

based on thin $In_{0.49}Ga_{0.51}P$ barriers to allow carrier tunneling. The EQE of 20-period lattice-matched $In_{0.38}Ga_{0.62}As_{0.34}P_{0.66}$ ($t_w = 44$ Å)/ $In_{0.49}Ga_{0.51}P$ ($t_b = 133$ Å), by Lee *et al*. [35], is depicted in Fig. 9(b). The inset shows the expected conduction band diagram of such structure. It is noted that the majority of the depletion region is occupied by the $In_{0.49}Ga_{0.51}P$ barriers. The P_{tun} and P_{therm} values in Table II indicate that the carriers are swept across the QW region by drift through thermionic emission due to using thin-wells.

In both the strain-balanced design, shown in Fig. 9(a), and the thick-barrier lattice-matched structures, shown in Fig. 9(b), the thickness of the absorbing InGaAsP well is about 25% of the total QW region thickness. This indicates that if the total thickness of the QW i region is 1 μm, only 250 nm will be absorbing the light. One strategy to address this is to increase the number of QWs; however, this is typically accompanied by limitations associated with drift-assisted carrier collection and epitaxial growth challenges such as strain-balance and CLT. In addition, the presence of unintentional background doping in the QW region affects the electric field distribution as will be discussed in Section VI.

To address that limitation, in a recent work, Sayed *et al*. grew thicker InGaAsP wells, and enabled carrier

tunneling through using thin $In_{0.49}Ga_{0.51}P$ barriers [41]. The EQE of 100-period lattice-matched $In_{0.32}Ga_{0.68}As_{0.55}P_{0.45}$ ($t_w = 55$ Å)/ $In_{0.49}Ga_{0.60}P$ ($t_b = 25$ Å) is shown in Fig. 9(c). It is noted that more than 60% of the period is occupied by the absorbing $In_{0.32}Ga_{0.68}As_{0.55}P_{0.45}$ wells. Modeling of tunneling and thermionic-emission probabilities, $P_{\mathrm{tun.}}$ and P_{therm}, for this QW design show the dominant presence of carrier tunneling over the thermionic emission of this structure, as shown in Table II. The EQE shows major improvements over the two initial QW designs. It should be mentioned that increasing the number of QWs should correspond to more improvements in the sub-bandgap EQE. The one-sun AM1.5 current density–voltage curve measured for the 100-period device is shown in Fig. 10(a). A schematic of the QW structure is also depicted in the inset of Fig. 10(a). The J_{sc}, V_{oc}, FF, and η of the 100-period $In_{0.32}Ga_{0.68}As_{0.55}P_{0.45}/In_{0.49}Ga_{0.60}P$ QW device were 18.5 mA/cm^2, 1.126 V, 72.3%, and 14.7%, respectively. The reported J_{sc} for the QW device is ~27% higher than an upright InGaP device that does not have QWs ($J_{\mathrm{sc}} = 14.8$ mA/cm^2) [88]. The reason for J_{sc} enhancement is due to the sub-bandgap absorption by the QWs and extending the absorption threshold to ~1.52 eV as shown in the EQE of Fig. 9(c). More details about the structures, shown in Fig. 9, such as the presence of window,
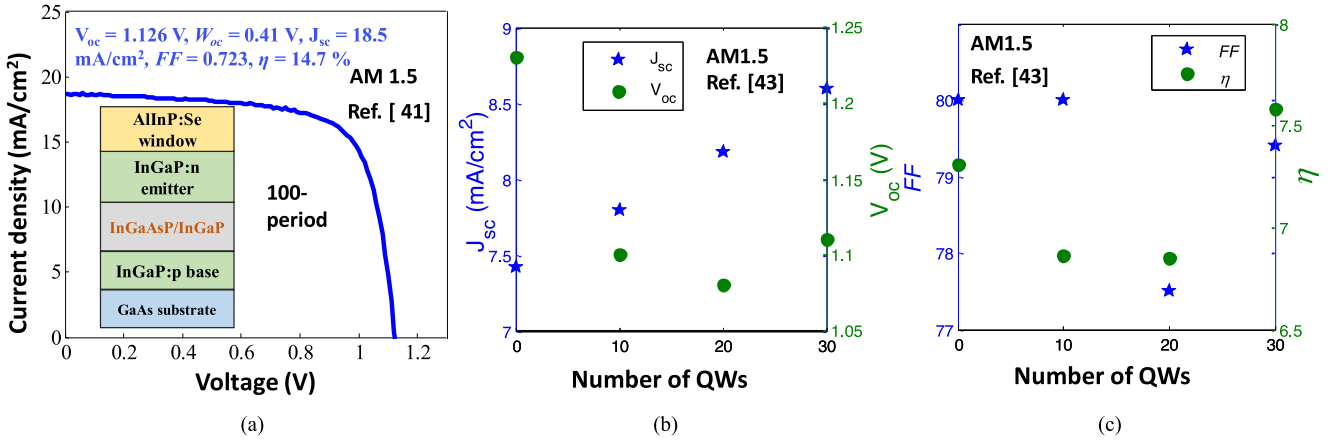
Fig. 10. (a) AM1.5 current–voltage characteristics of lattice-matched $In_{0.32}Ga_{0.68}As_{0.55}P_{0.45}$ ($t_w = 55$ Å)/ $In_{0.49}Ga_{0.60}P$ ($t_b = 25$ Å), with the inset showing a schematic of the QW structure by Sayed *et al.* [41]. The effect of the number of QWs in strain-balanced $In_{0.70}Ga_{0.30}As_{0.05}P_{0.95}$ (45 Å)/$In_{0.40}Ga_{0.60}P$ (140 Å) on AM1.5 one-sun current–voltage characteristics. (b) J_{sc} (mA/cm^2) and V_{oc} (Volts). (c) FF and η; study by Hashem *et al.* [43].

back surface field, or antireflection coatings are discussed in the references.

The effect of the number of the period on strain-balanced $In_{0.70}Ga_{0.30}As_{0.10}P_{0.90}$ ($t_w = 45$ Å)/$In_{0.40}Ga_{0.60}P$ ($t_b = 140$ Å) QW is depicted in Fig. 10(b) and (c), using the tabulated data reported by Hashem *et al.* [43]. The increase of the QW number enhances the J_{sc} due to increasing the total thickness of absorbing layers, see Fig. 10(b). The V_{oc} does not vary significantly with the period change, as shown in Fig. 10(b). The FF exhibits a slight deterioration due to an increase in the number of interfaces, see Fig. 10(c). The efficiency of the 30-period strain-balanced InGaAsP/InGaP QW solar cell is 7.57%, which is slightly higher than the efficiency of the standard In-GaP device (7.3%) used in this study, that does not include QWs, as shown in Fig. 10(c). It should be mentioned that increasing the number of QWs from 30 to 45 was accompanied by a degraded performance due to exceeding the depletion region thickness [43]. Thus, achieving an InGaAsP/InGaP QW device with a high number of periods with an efficiency higher than the standard $In_{0.49}Ga_{0.51}P$ cell requires further optimization.

It should be mentioned that there are several challenges with the growth of this QW structure. First, it is challenging to grow high-quality InGaAsP layer with compositions within the miscibility gap. InGaAsP with compositions within the miscibility gap has a tendency to decompose through the spinodal decomposition mechanism and separates into InAs and GaP rich regions [16], [89], [90]. This phase separation is more significant for thick bulk InGaAsP and degrades the diffusion length and the optical characteristics of solar cells. It was reported that using thin strained InGaAsP can impede this phase separation [91]. Hence, the lattice-matched and strain-balanced InGaAsP/InGaP structures used a relatively thin InGaAsP well to reduce the driving forces of the miscibility gap. Second, it is challenging to grow a 100-period device in terms of crystal growth because of the possible presence of defects at the interfaces. The third challenge with InGaAsP/InGaP QW structure arises due to the fact that indium compositions in the well and barrier are not the same. Hence, the indium flow will be ramped up or down to grow

well and barrier. Ramping up or down any of the flows may result in a degraded interface between the well/barrier and/or the barrier/well. The fourth challenge is related to switching the arsenic on and off, which might result in the presence of interfacial InGaAsP layers with unknown compositions of a few monolayers thickness.

To address some of these challenges, Sayed *et al.* carried out growth modifications in the lattice-matched 100-period In-GaAsP/InGaP, shown in Fig. 9(c) [92]. First, the growth temperature was optimized to reduce the driving forces of miscibility; and growth temperatures less than 650 °C were reported, by Jain *et al.*, to induce ordering effects, which suppress the InGaAsP decomposition [81], [93]. Thus, this has allowed the growth of much thicker InGaAsP occupying 60% of the total QW thickness. The stress buildup during growth was monitored using *in situ* curvature, and the arsenic to phosphorus ratio was changed to obtain nearly strain-free structures. To keep all the flows fixed during growth, different gallium precursors in wells and barriers were used and a fixed indium flow was used. To address the arsenic ON/OFF switching issue, a growth pause of phosphine was employed [92].

C. Strained InGaN/GaN Quantum Wells to Achieve a > 2.1 eV Subcell

Strained InGaN/GaN QWs are grown in the unintentionally doped i layer of GaN n-i-p solar cells as shown in Fig. 1(c). The emitter and base are GaN doped typically with magnesium and silicon, respectively. InGaN-based alloys have received tremendous attention for use in photovoltaic devices in the last few years [13], [44]–[47], [59], [94]. This interest has been driven by favorable properties of InGaN-based alloys, including a direct band gap ranging from 0.64 eV for InN to 3.4 eV for GaN, high absorption coefficients of 10^5 cm^{-1} near the band edge, as well as high resistance to high energy photon irradiation [59], [95]. $In_{0.45}Ga_{0.55}N$ is also proposed as a potential topcell that can be mechanically stacked with Si in tandem solar cells to achieve η higher than 31% [96]. In addition, developing InGaN
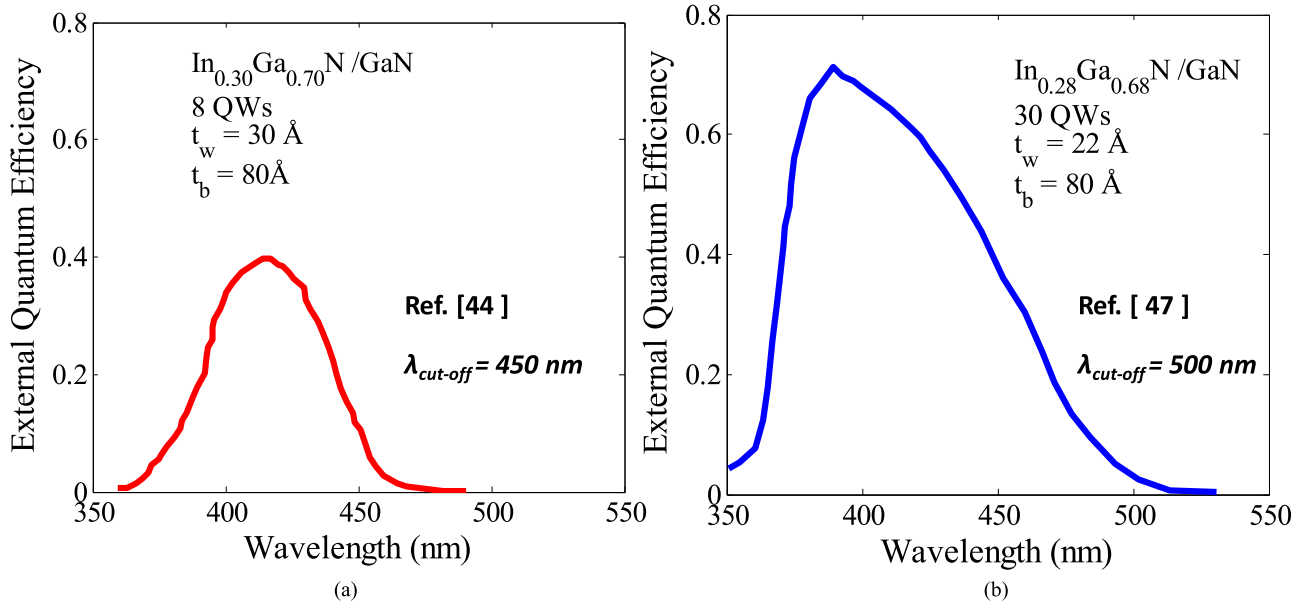
Fig. 11.   External quantum efficiency of InGaN/GaN QW solar cells with high indium fraction ($x > 0.2$). (a) Eight periods of $In_{0.30}Ga_{0.70}N$ ($t_w = 30$ Å)/GaN ($t_b = 80$ Å) that has a cut-off wavelength at ~450 nm, by Dahal *et al*. [44]. (b) 30-period $In_{0.28}Ga_{0.72}N$ ($t_w = 22$ Å)/GaN ($t_b = 80$Å) that has a cut-off wavelength at ~500 nm by Farrell *et al*. [47], that includes heavily doped GaN layers to help in screening the polarization-induced in the QW region and rough GaN window to reduce front reflection.

with bandgap higher than 2 eV is important for next generation five (or more) junction devices [13], [44]–[47], [59].

The EQE responses of two structures that have indium percentage higher than 20% are reviewed because a bandgap in the 2.0–2.5 eV is required for next generation (five or more) photovoltaic devices. Fig. 11(a) shows the EQE of 8-period of $In_{0.30}Ga_{0.70}N$ ($t_w = 30$ Å)/GaN ($t_b = 80$ Å) that has a cut-off wavelength ($\lambda_{cut-off}$) at about 450 nm, by Dahal *et al*. [44]. Beyond the band-edge of GaN (365 nm), absorption occurs only in the $In_{0.30}Ga_{0.70}N$ QW and the quantum efficiency is limited to less than 10% at 450 nm due to several reasons. First, the total thickness of absorbing $In_{0.30}Ga_{0.70}N$ well is only 24 nm, which is very thin to achieve high EQE values. Second, the presence of high lattice-mismatch between GaN and InN of ~11.8% results in highly strained InGaN films especially for compositions higher than 20%, thus resulting in a highly defective material. This degrades the InGaN film quality and degrades the optical characteristics of the solar cell. Third, the use of high indium percentage results in high polarization field which opposes the carrier collection. To address some of the earlier challenges, Farrell *et al*. proposed 30-period $In_{0.28}Ga_{0.72}N$ ($t_w = 22$ Å)/GaN ($t_b = 80$Å) grown in a GaN p-i-n solar cell, see Fig. 11(b) [47]. The growth of 30-periods increases the thickness of absorbing $In_{0.28}Ga_{0.72}N$ well to 66 nm, which is higher than the earlier work by Dahal *et al*., by a factor of 2.75. The active region, where the QWs are located, is surrounded by highly doped GaN:p and GaN:n layers to assist in screening the polarization-induced field in the QWs which opposes the carrier collection [97], [98]. In addition, to reduce the air/GaN reflection, a roughened GaN:p surface was grown to increase the path length of the light. These enhancements have resulted in EQE values exceeding 60% at 400 nm as shown in Fig. 11(b)

and the absorption threshold was extended to ~500 nm. The 1.2 suns AM1.5 current density–voltage curve measured for the 30-period $In_{0.28}Ga_{0.72}N$/GaN QW device, by Farrell *et al*. [47], is shown in Fig. 12(a). A schematic of the structure is also depicted in the inset of Fig. 12(a). The J_{sc}, V_{oc}, FF, and η of the 30-period $In_{0.28}Ga_{0.72}N$/GaN QW device, by Farrell *et al*. [47], were 2.53 mA/cm^2, 1.93 V, 56.4, and 2.29%, respectively. Even with the EQE improvement shown in Fig. 11(b), the reported η is still low because of the low J_{sc} value due to the thin absorbing $In_{0.28}Ga_{0.72}N$ layer (66 nm), and also the QWs are absorbing in a narrow wavelength region in the solar spectrum. The V_{oc} is markedly high, relative to III/V materials, due to the high bandgap of InGaN/GaN.

The effect of the number of the period on strained $In_{0.28}Ga_{0.72}N$/GaN QW is depicted in Fig. 12(b) and (c), using the tabulated data reported by Farrell *et al*. [47]. The increase of the QW number enhances the J_{sc} due to increasing the total thickness of absorbing layers, see Fig. 12(c). The V_{oc} does not vary significantly with the period change, as shown in Fig. 12(b). The FF exhibits a slight deterioration due to an increase of number of interfaces, see Fig. 12(c). The overall efficiency of the device increases with the increase of the number of QWs, as shown in Fig. 12(c).

According to several calculations and experimental investigations for InGaN/GaN structures with different well/barrier thickness and indium compositions, the major carrier escape in this QW structure is tunneling [99]–[101]. The thermionic emission is less dominant for the InGaN/GaN due to the relatively high effective barrier height for the electrons and holes, especially with high indium percentage. For instance, the τ_{tun} is ~10^{-10} s for $In_{0.17}Ga_{0.83}N$ ($t_w = 30$ Å)/GaN ($t_b = 100$ Å) which is about 100-times lower than the $\tau_{therm.}$ (~10^{-8} s) as reported
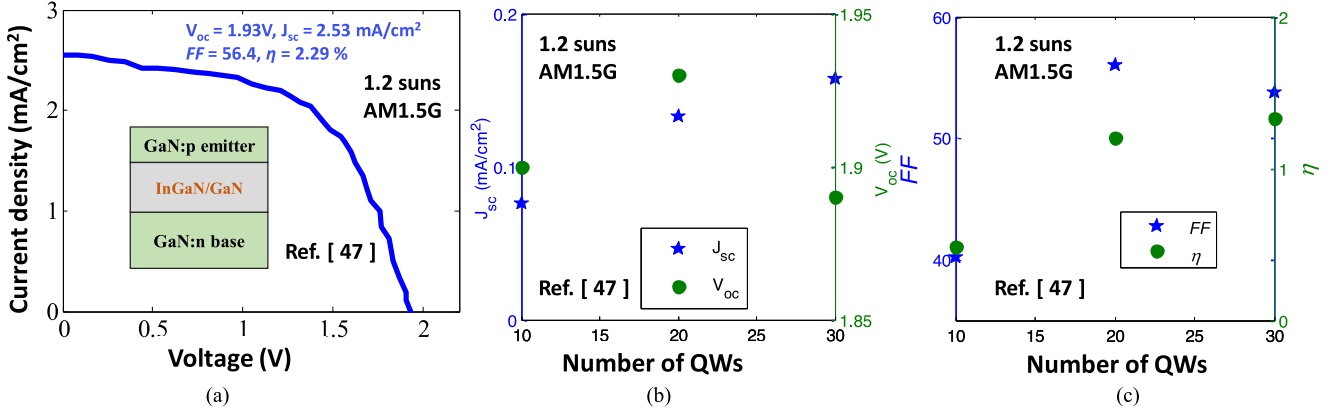
Fig. 12. (a) 1.2 suns AM1.5 current–voltage characteristics of 30-period $In_{0.28}Ga_{0.72}N$ ($t_w = 22$ Å)/GaN ($t_b = 80$Å) by Farrell *et al.* [47], with the inset showing a schematic of this structure. The effect of the number of QWs in the intrinsic region on 1.2-suns AM1.5G current–voltage characteristics. (b) J_{sc} (mA/cm^2) and V_{oc} (Volts). (c) FF and η; study by Farrell *et al.* [47].

by Lang *et al.* [100]. For a fixed well and barrier thickness, increasing the indium percentage in the InGaN will degrade carrier collection for several reasons. First, the use of higher indium percentage will increase the effective barrier height resulting in a reduction in both the tunneling and thermionic escape probabilities, see (10) and (11). For instance, the tunneling and thermionic-emission escape times, τ_{tun} and $\tau_{therm.}$, are more than 100-times higher in $In_{0.25}Ga_{0.75}N$/GaN than their corresponding values in $In_{0.17}Ga_{0.83}N$/GaN. Second, an increase in the indium from 17% to 25% increases the piezoelectric field from 1.74 to 2.3 MV/cm, which will result in a more opposition of carrier collection.

There are several challenges that hinder the fabrication of high-quality InGaN-based QW devices. The most challenging issue is the growth of high-quality InGaN with high indium percentage exceeding 20%. InGaN with more than 20% indium results in a poor solar cell performance due to the formation of high defect density and pits that results in a high non-radiative recombination, increases the dark current, and degrades the V_{oc} and η. The difficulty of InGaN with high indium percentage is attributed to the large difference in the interatomic spacing between GaN and InN thus resulting in a solid-phase miscibility gap [102]–[104]. Second, there is a lattice-mismatch between GaN and InN on sapphire substrates of −16% and +29%, respectively. Also, the difference in thermal expansion coefficients between epilayer and substrates causes a thermal strain that introduces threading dislocations in the epilayer. To address this issue, a GaN template is typically grown as shown in Fig. 1(c); however, this will not eliminate the lattice mismatch between the InGaN epilayer and GaN template. The latter mismatch will increase with the increase of indium percentage in the well. One possible strategy to address this issue is to grow a relaxed $In_yGa_{1-y}N$ template on GaN and then grow strain-balanced $In_xGa_{1-x}N$/GaN, with $In_xGa_{1-x}N$ well and GaN grown under compressive stress and tensile stress to the underlying $In_yGa_{1-y}N$ template, respectively, where $x > y$ [48], [105]. However, only LEDs were fabricated using this approach, and solar cells using the strain-balanced InGaN/GaN approach have not been developed yet [48], [105], [106]. The

third challenge is to grow GaN with a hole concentration exceeding 1×10^{18} cm^{-3} to act as a p-type emitter and ohmic contact when the metal is evaporated [107]. Magnesium (Mg), which is an acceptor in GaN, has a high activation energy of 0.2 eV that will limit the doping concentration [108]. The activation energy of Mg in GaN decreases with the increase of indium percentage thus allowing high p-type doping than GaN. Finally, most research in InGaN/GaN QW solar cells has focused on developing p on n structures. However, high-performance III/V and silicon subcells have an n on p polarity. The growth of n on p results in built-in and polarization fields in the same direction, which is a problem due to the high sheet resistance of GaN:p and low mobility [59]. Hence, this also represents a challenge that needs to be addressed for developing hybrid tandems that incorporate InGaN-based QWs as a top cell material.

V. COMPARISON OF QUANTUM WELLS' PERFORMANCE WITH BULK ABSORBERS

In this section, the performances of the state-of-the-art EQE results of the three discussed QWSC in Fig. 1 are compared with bulk absorbers operating in a bandgap range close to the QWs. For the 1.1–1.3 eV range, metamorphic InGaAs bulk subcell grown on Ge (or GaAs) substrates by Spectrolab [109] is compared with 100-period $In_{0.30}Ga_{0.70}As$(3.5 nm)/GaAs(2.7 nm)/$GaAs_{0.60}P_{0.40}$(3.0 nm) QWSC by Fujii *et al.* [25], see Fig. 13(a). The two lattice-mismatched InGaAs, shown in Fig. 13(a), have high EQE values at the absorption threshold near the band-edge, which indicates high minority diffusion length. The InGaAs subcells show higher EQE values than the QWs in the 880–980 nm. The InGaAs metamorphic shows a higher potential than QWs for extending the absorption threshold to longer wavelengths. The latter is due to the fact that extending the absorption threshold of QWs to longer wavelengths requires careful management of CLT, strain balance, and carrier transport issues, as discussed in Section III. However, bulk grown InGaAs has a high density of defects, which will degrade the quality of the top cell such as InGaP-based cells grown on the InGaAs bottom cell. There has been a lot of effort to reduce the defects in these
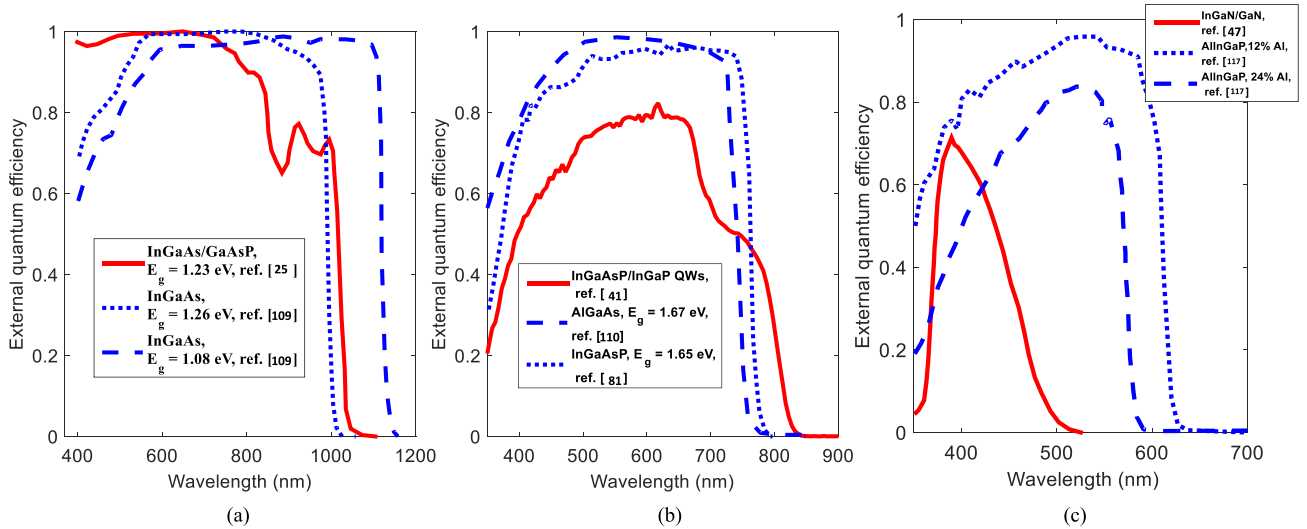
Fig. 13.   Comparison of the three discussed QW solar cells with bulk absorbers. (a) EQE of InGaAs/GaAsP by Fujii *et al.* [25] (shown in red) and InGaAs subcells with different bandgap values (shown in **blue**) grown inverted on a metamorphic buffer by Spectrolab [109]. (b) EQE of InGaAsP/InGaP by Sayed *et al.* [41] (shown in red), and AlGaAs by Heckelmann *et al.* [110] and InGaAsP by Jain *et al.* [81] that are lattice matched to GaAs substrate (shown in **blue**). (c) EQE of InGaN/GaN by Farrell *et al.* [47] (shown in red) and AlInGaP lattice matched to GaAs by Perl *et al.* with different aluminum compositions (shown in **blue**) [116], [117]. Limitations and issues related to bulk films of InGaAs, AlGaAs, InGaAsP, and AlInGaP in tandem structures are addressed in the text. More details about these structures such as the presence of window, back surface field or antireflection coatings are discussed in the references.

films, however, low minority carrier lifetime was reported for the top cell in the tandem InGaP/InGaAs structure. The minority carrier lifetime problem was recently addressed by the inverted metamorphic structure, where the high bandgap cell, InGaP, was grown first, followed by a compositionally graded transparent buffer to grow InGaAs bottom cell [23]. This approach requires extra effort of etching the GaAs substrate. The strain-balanced InGaAs/GaAsP QW approach with a bandgap of 1.2 eV is lattice matched to GaAs substrates and the tandem solar cell is grown under upright conditions without any extra fabrication steps. The InGaAs/GaAsP QW approach can be easily integrated with the bottom Ge solar cell, thus offering better mechanical stability for the tandem structure. Recent efforts by NCSU/Spectrolab have shown the successful integration of $In_{0.49}Ga_{0.51}P$ (1.9 eV) top cell with GaAs bottom cell that incorporates InGaAs/GaAsP QWs [39].

For the 1.6–1.8 eV range, the performance of lattice-matched AlGaAs by Heckelmann *et al.* [110] and InGaAsP by Jain *et al.* [81] is compared with the lattice-matched InGaAsP/InGaP QW structure by Sayed *et al.* [41]. The EQE of InGaAsP and AlGaAs is higher than the InGaAsP/InGaP QWSC in the longer wavelengths as shown in Fig. 13(b). The QW structures are grown at low temperatures (550–600 °C) less than that of high-performance AlGaAs (640 °C) [110] and bulk InGaAsP cells (600—650 °C) [81], [93]. The low-temperature growth of QWs prevents any thermal degradation of the connecting tunnel junction grown underneath the subcell [111]–[113]. Also, the growth of AlGaAs solar cell was only successful by very few research groups [9], [110]. AlGaAs is indirect for aluminum compositions higher than 45%. The InGaAsP/InGaP QW approach can be easily tuned to any desirable bandgap by scaling the well/barrier thickness, as shown in Fig. 3(b). It is not clear yet if the corresponding bulk grown InGaAsP can be tuned to the wide range that the QW can access.

The performance of InGaN/GaN and AlInGaP (Al = 12% and Al = 24%) is compared in Fig. 13(c). The development of AlInGaP has been historically problematic due to the high reactivity of aluminum with oxygen thus creating deep level centers and reduced minority carrier lifetime [114], [115], which will degrade the solar cell performance. Recently, high-performance 2.1 eV AlInGaP solar cells have been developed by Perl *et al.* [116], [117], which will be used as the highest energy subcell in five- and six-junction devices [9], as shown in Fig. 13(c). However, growing AlInGaP at temperatures higher than 700 °C is mandatory to minimize oxygen contamination. Such high temperatures may enhance dopants diffusion in the tunnel junction thus resulting in a degraded tunnel junction performance under thermal load [111]. It is noted that increasing the Al% to 24 resulted in a lower performance device due to the possible presence of more defects and the unavailability of higher bandgap lattice-matched windows layer. In order to realize a cell with bandgap higher than 2.33 eV, which is crucial for seven (or more) junction devices, AlInGaP will be indirect and aluminum percentage higher than 30% will be mandatory which might result in higher recombination centers and weaker absorption. Hence, it becomes important to address the challenges associated with InGaN-based solar cells for potential use in next-generation seven (or more) photovoltaic devices.

VI. EFFECTS OF BACKGROUND DOPING AND ELECTRIC FIELD ON CARRIER COLLECTION

In this section, the effects of background doping on the carrier collection by drift will be addressed using modeling and experimental results. This background doping issue limits the use of a high number of periods in QW devices. Ideally, these QWs are grown undoped, but an unintentional background doping in the order of 10^{15} –10^{16} cm^{-3} exist during the growth
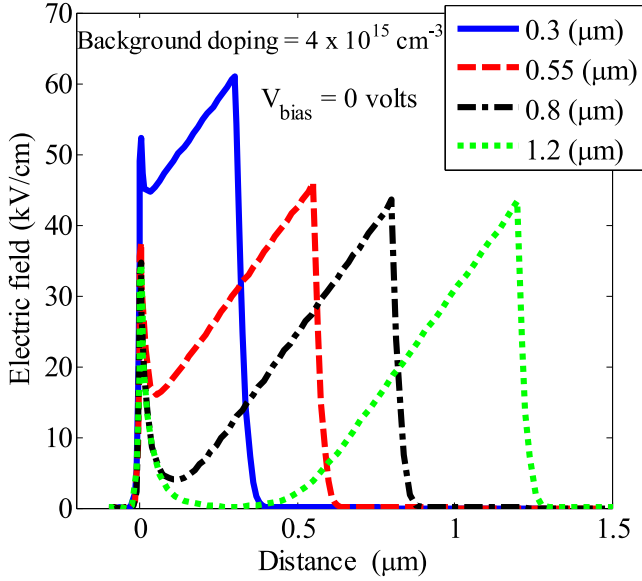
Fig. 14. Effect of increasing the QW region thickness on the electric field distribution at short-circuit condition (i.e., zero bias). A background doping of 4×10^{15} cm^{-3} p-type is assumed here.

of these structures. The unintentional background doping in the GaAs-based materials and GaN-based materials, grown by metal organic chemical vapor deposition, are typically p-type and n-type, respectively. Also, it has been reported that radiation induces damage that is responsible for changing the doping concentration in the QW region [36], [118]–[120]. It is believed that the radiation induces crystal defects within the forbidden gap and creates trap states that can localize free carriers, resulting in the so-called carrier removal. It is also believed that radiation-damage typically results in N-type carriers in the QW region [36], [121].

The presence of an unintentional background doping in the QW region can create another junction between QWs and the counter-doped side, and hence weakens the electric field distribution in the QW region and results in SRH recombination centers [70]. In order to highlight the background doping issue, the electric field distribution is modeled using a physics-based software PC1D [122]. The dielectric function of QW medium region is modeled by averaging the permittivity of the well and barrier as given by Aspnes formula [36], [123]. Fig. 14 shows the electric field distribution for a GaAs(p)-InGaAs/GaAsP QW-GaAs(n) structure with a p-type background doping of 4×10^{15} cm^{-3} in the QW region, with various QW region thickness at short-circuit condition (i.e., zero bias). For an intrinsic QW device, the electric field is uniform, implying all the electron-hole pairs generated in the QW region can effectively be swept across the device. However, the presence of the background doping results in a weak or zero electric field region which will degrade the carrier collection by drift as shown in Fig. 14. For a QW device with a background doping of 4×10^{15} cm^{-3}, as shown in Fig. 14, as the number of QWs increases, a wider region of weak or zero electric field which inhibits the drift carrier collection would exist. As the background doping increases, the width of this region will increase. The maximum depletion

region thickness versus the doping concentration in the QW is shown in Fig. 15(a) at the short-circuit condition (i.e., zero bias). The total QW region thickness that can be grown depleted is 4.2, 1.35, 0.45 μm for doping concentrations of 10^{16}, 10^{15}, 10^{14} cm^{-3}, respectively, as shown in Fig. 15(a). The growth of undepleted QWs will limit the carrier collection (by drift), thus limiting the sub-bandgap quantum efficiency. Hubbard Group at RIT showed that the SRH recombination is more dominant away from the middle of the quantum dot (QD) region for a high background-doping QD device [124].

To address this issue, researchers in the QW and QD fields have studied the effect of QW (dot) location on the performance of solar cell devices by changing the position of the QW (dot) in the i layer [124]–[126], and showed that placing the QWs (dots) away from the high recombination region results in less dark current and higher V_{oc}. However, no device with high EQE values beyond the sub-bandgap has been fabricated using this approach, possibly due to the limited number of QWs that can be included.

In order to address the background doping issue, researchers at the University of Tokyo and NCSU have investigated the effect of counter-doping the p-type QW region using silicon or sulfur to reduce the background doping to 10^{14} cm^{-3} to obtain a more uniform electric field distribution. Fig. 15(b) shows new results, by the NCSU group, for the doping in the QW region versus the disilane flow. The carrier concentration was measured by capacitance–voltage (CV) measurements. The region above and below zero x-axes represent p-type and n-type concentration, respectively. The p-type concentration was reduced from $\sim 7 \times 10^{15}$ cm^{-3} to 5×10^{14} cm^{-3} using a disilane flow of 25.6 μmol/min, as shown in Fig. 15(b). This will correspond to a ~ 1.9 μm depletion region as indicated by Fig. 15(a). Also, the reduction of the background doping to 5×10^{14} cm^{-3} indicates the potential of the growth of ~ 143-period device of In$_{0.18}$Ga$_{0.82}$As (100 Å)/GaAs$_{0.36}$P$_{0.64}$ (32 Å). Similar results were achieved by Fujii et al. using sulfur [127]. Fig. 16(c) shows external quantum efficiency results, by Fujii et al., for In$_{0.3}$Ga$_{0.7}$As(32 Å)/GaAs (2.7 Å)/GaAs$_{0.6}$P$_{0.4}$ (50 Å)/GaAs (27 Å) grown at temperature of 530 °C [128]. The unintentional p-type doping in that experiment was 1×10^{17} cm^{-3} for the QWs grown at 530 °C, which will limit the depletion region to about 0.15 μm, as shown in Fig. 16(a). Hence, the EQE of the 50-period QW device (~ 0.68 μm), shown in Fig. 15(c), was very poor due to the weak electric field distribution as implied by Fig. 14. However, the compensation doping of the p-type QW region with sulfur resulted in a net doping less than 10^{15} cm^{-3}, which had extended the depletion region to ~ 2 μm and resulted in the major EQE improvements shown in Fig. 15(c). Based on our experiences with such experiments, it is complicated to control the doping to the 10^{14} cm^{-3} level, and hence reproducing some of these results is challenging.

A more practical and reproducible approach to address the background doping issue is to use precursors that may result in less p-type incorporation. The p-type contamination is due to surface reactions of trimethyl-gallium (GaCH$_3$), that produce GaCH$_2$ which reacts with surface gallium atoms to produce carbon on an arsenic site [16], [129]. Thus, the pyrolysis

(a)   (b)   (c)
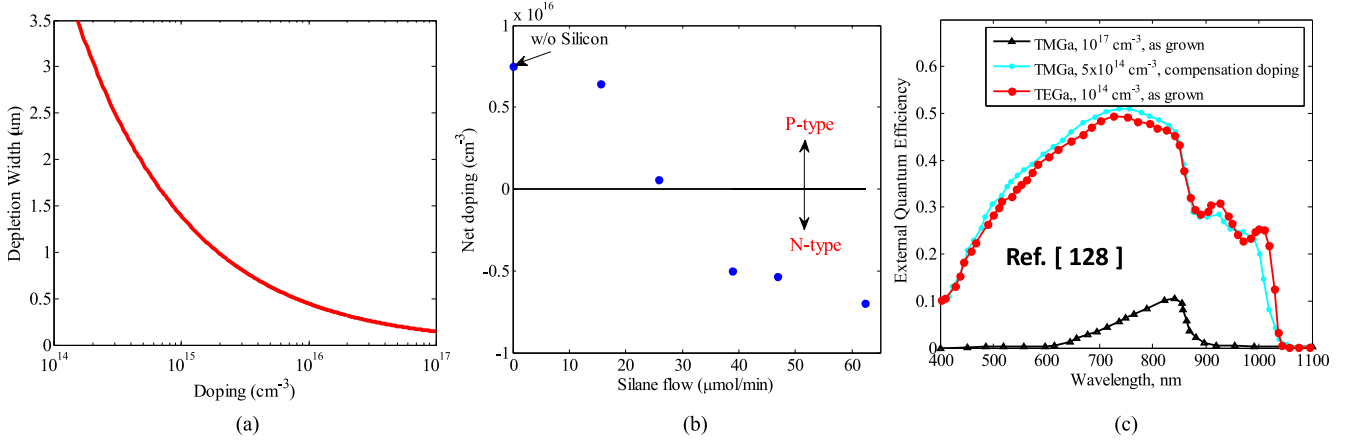
Fig. 15. (a) Simulation of the maximum depletion width as a function of p-type background doping at short-circuit condition (i.e., zero bias). The intrinsic carrier concentration (n_i) used was 1.79×10^6 cm^{-3}. (b) Measured net doping in the QW region as determined by capacitance–voltage (CV) measurements, versus the disilane flow. (c) External quantum efficiency of two InGaAs/GaAsP QW devices that use TMGa as a gallium precursor; one is compensated with sulfur and the other is unintentionally doped of 10^{17} cm^{-3}, as well as an InGaAs/GaAsP QW device that uses TEGa as a gallium precursor, by Fujii et al. [128].
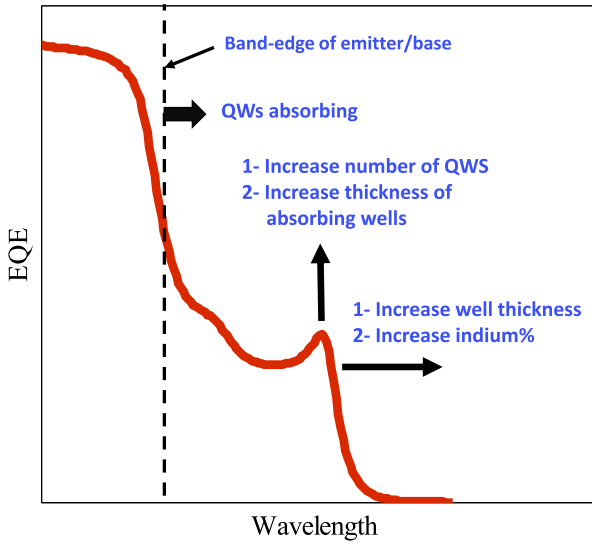

Fig. 16. External quantum efficiency versus wavelength, showing the potential strategies for enhancing the quantum well quantum efficiency of QW solar cell devices. The vertical dotted line is the band-edge of emitter/base. The region beyond the band-edge is where the QWs are absorbing.

of trimethyl-gallium (TMGa) forms methyl-radicals that are absorbed on the surface at low temperature, causing severe carbon incorporation and the p-type background doping. The temperature dependence of carbon incorporation is related to the competition between the relative rates of hydrogen (H) loss and the production of CH$_4$ that can be rapidly desorbed [130]. Hence, the carbon concentration also increases at low temperatures of <600 °C [16], which is close to the temperatures at which QWs are typically grown. A strategy to address this issue is to use triethyl-gallium (TEGa) as a gallium precursor instead of TMGa. The main reaction product observed by Yoshida et al. [131] was ethylene, which indicates that the pyrolysis occurs mainly by the β-hydride elimination mechanism [128], [132]

$$\mathrm{Ga(C_2H_5)_3} \longrightarrow \mathrm{GaH(C_2H_5)_2 + C_2H_4.} \qquad (14)$$

The pyrolysis occurs via the reaction of (14) results in no ethyl-radicals [133], [134]. This reduces carbon incorporation, increases the depletion layer thickness, and allows more QWs to be grown in the high electric field region [128], [130], [132]. Based on experiments by Fujii et al. [128], a carbon concentration in the order of 10^{14} cm^{-3} can be realized using TEGa as a gallium precursor in the GaAsP and InGaAs layers. The EQE of the InGaAs/GaAsP, using TEGa as a gallium precursor, is similar to that obtained by sulfur compensation doping as shown in Fig. 16(c).

VII. CHALLENGES AND POTENTIAL

In this section, the challenges with developing higher efficiency QWSC and the potential for incorporating QWs in next-generation multi-junction devices are discussed. There are two main issues that need to be addressed to realize high-efficiency solar cells that incorporate QWs, as shown in Fig. 16: 1) enhancing the QW EQE to higher values, and 2) extending the absorption threshold to longer wavelengths (lower energies) to optimize the bandgap.

There are two main strategies to enhance the QW EQE: 1) increasing the number of QWs, and 2) increasing the thickness of the absorbing QW relative to the barrier, see Fig. 16. First, an increase in the number of QWs improves the short-circuit current and efficiency as discussed in Figs. 8, 10, and 12. There are three main issues that challenge the high number of QWs growth and few potential strategies to address these challenges.

1) Stress management issue: Increasing the number of QWs requires proper management of stress buildup during growth. This is because increasing the number of interfaces might induce defects/dislocations, which degrade the efficiency if the strain-balance condition was not fully realized. This requires adjusting the thicknesses of wells/barriers as well as the compositions to realize the strain-balance condition, as discussed in Section III-C. In order to address the stress management issue, researchers

have used approaches like *in situ* curvature and reflection measurements to estimate the stress build-up during growth using Stoney's equation [92], [135]–[137]. These techniques can offer the flexibility of adjusting the growth conditions in the middle of the experiment to manage the stress. For example, if the net stress during the growth of the first few QWs in InGaAs/GaAsP is tensile, the thickness of InGaAs should be increased or the GaAsP should be decreased, in order to balance the tensile stress by a compressive stress.

2) Carrier transport issue: The second issue that needs to be addressed with increasing the number of QWs is to guarantee efficient carrier collection across the QW region. For instance, the tunneling probability ($P_{\text{tun.}}$) for heavy holes of a single $In_{0.32}Ga_{0.68}As_{0.55}P_{0.45}/In_{0.49}Ga_{0.51}P$ (40 Å) QW is 99.2%. Increasing the number of QWs to 20 and 100 will lead to a tunneling probability of 85.1% and 44.67%, respectively. Hence, this indicates the QW design is not fully optimized to guarantee carrier collection by drift for the heavy holes in the 100-period QW device. To address this issue, the layers' thicknesses should be optimized to increase the probabilities for tunneling and thermionic-emission. For example, reducing the $In_{0.49}Ga_{0.51}P$ barrier thickness from 40 to 25 Å will enhance the probability of tunneling from 44.67% to 98.48% across the 100 QWs, thus indicating the heavy holes can be efficiently collected.

3) Electric field and background doping issue: Increasing the number of QWs might result in including few QWs in a region where the electric field is very low, as shown in Fig. 14. It is thus crucial to guarantee a uniform electric field distribution across the QW region, as discussed in Section VI. Hence, strategies such as reducing the background doping through compensation doping or use of precursors that result in less p-type contamination might be essential to guarantee both efficient light absorption and carrier collection, as discussed in Section VI.

The second strategy that leads to enhancing the QW EQE is to increase the percentage of absorbing well thickness relative to the barrier thickness and using thin barriers to enable carrier tunneling, as discussed for some of the structures in Section IV. For instance, the use of 100-period $In_{0.11}Ga_{0.89}As$ (93 Å)/$GaAs_{0.93}P_{0.07}$ (160 Å) results in a total absorbing $In_{0.11}Ga_{0.89}As$ thickness of 0.93 μm and total QW region thickness of ~2.5 μm. However, the use of a structure which relies on high-phosphorous in the barrier, such as $In_{0.14}Ga_{0.86}As$ (115 Å)/$GaAs_{0.24}P_{0.76}$(27 Å), and growing an 80-period device will result in the same total absorbing InGaAs thickness (~0.93 μm) with much thinner QW region (~1.13 μm). Thus, this will allow a further increase in the number of QWs to enhance the quantum-well EQE. It is also worth pointing out that the well thickness should be kept less than the CLT as discussed in Section III-B.

If the two previously mentioned strategies are combined, increasing both the number of QWs and the thickness of absorbing wells, this should correspond to a major enhancement in the QW EQE.

To extend the absorption threshold to longer wavelengths, two main strategies can be followed: 1) increasing the QW thickness to reduce quantum size effects, and 2) increasing the indium percentage in the QW. The well-thickness/indium-content increase might have negative effects on the performance of the QW solar cell, if not addressed properly. The first effect is an increase in the compressive stress which might result in a violation of strain-balance condition if tensile stress was not increased to strain-balance the QW structure. This can be addressed in any strain-balanced QW structure, such as InGaAs/GaAsP and InGaAsP/InGaP, by adjusting the compositions and the thicknesses of GaAsP and InGaP barriers to meet the strain-balance condition. However, increasing the thickness or indium percentage in strained InGaN/GaN might degrade the InGaN film quality especially for indium compositions higher than 20%. The second effect, due to well-thickness/indium-content increase, is the increase in the effective barrier height for both the electrons and heavy holes to maintain the strain-balance condition. This will reduce the tunneling and thermionic-emission probabilities, as implied by (10) and (11), and will affect the carrier collection (by drift).

To address the increase in the barrier height issue, a barrier of composition that is closer to the lattice constant of GaAs substrate can be used. This is more effective in a QW structure that relies on thermionic emission carrier transport. For example, strain-balanced $In_{0.73}Ga_{0.27}As_{0.05}P_{0.95}$ (45 Å)/$In_{0.32}Ga_{0.68}P$ (150 Å) structure has a barrier height for electrons of 0.188 eV and thermionic-emission probability for electrons across 50 QWs is 92.75%. If the well thickness was increased from 45 to 80 Å to enhance the QW EQE, the barrier height will also be increased from 0.188 to 0.2247 V and the thermionic emission probability will be reduced from 92.75% to 57.6%, which will degrade the device performance. If an $In_{0.45}Ga_{0.55}P$ barrier (80 Å) was used, instead of $In_{0.32}Ga_{0.68}P$(80 Å), the barrier height for $n = 1$ electrons will be reduced from 0.2247 to 0.15 V and this will enhance the thermionic emission probability to 96%. The thickness of the barrier should be adjusted in all structures to maintain the strain-balanced condition.

In addition to enhancing the QW EQE values and extending the absorption threshold, one has to deal with the challenges associated with each material system such as the phase separation issue in InGaAsP and InGaN, the group V switching issue in InGaAs/GaAsP system, and the difficulty of high-quality InGaN with 20% or higher indium as discussed in Sections III–V.

There are several potential applications for QWs in next-generation solar cell devices. These applications are driven by favorable properties of QWs, such as bandgap tunability, the growth of structures that are lattice matched to substrates, the low-temperature of growth of the QWs which prevents any thermal degradation of the tunnel junction, and the complexity of achieving high-efficiency bulk absorbers of similar bandgaps to QWs. The optimum bandgaps needed for subcells in 2–8 junction devices, under constrained AM1.5G, are shown in Fig. 17 [138]. The horizontal dotted lines in Fig. 17 represent the bandgap range that can be realized using the InGaAs/GaAsP, InGaAsP/InGaP, and InGaN/GaN. As shown in Fig. 17, there is a potential for using QWs in several multijunction devices. For
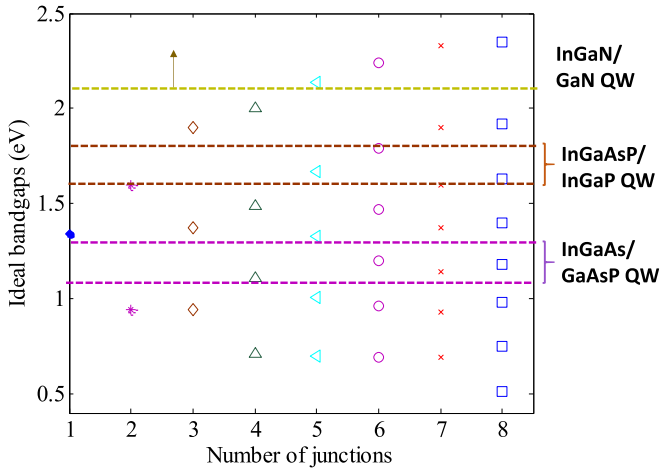
Fig. 17. Ideal bandgap energy for each junction in a multi-junction solar cell as the number of junctions is increased from one to eight. InGaAs/GaAsP, InGaAsP/InGaP, and InGaN/GaN quantum well solar cell structures can be used to realize the bandgap range identified by the horizontal dotted lines. The data for ideal bandgaps are plotted from [138].

example, strain-balanced or lattice-matched InGaAsP/InGaP can be used as a 1.6–1.8 eV subcell in five (or more) multi-junction cells. Also, if a 1.1 eV InGaAs/GaAsP structure is used as a bottom cell and a 1.7 eV InGaAsP/InGaP QW is grown on top of it, the two QWs will be grown strain-balanced to GaAs substrates and there will not be a need for a compositionally graded buffer as in the inverted metamorphic approach. It should be also mentioned that the use of AlInGaP might be inefficient for the subcells with bandgaps higher than 2.2 eV, as shown in Fig. 17, due to the unavailability of higher bandgap windows, which are lattice-matched to GaAs substrates. On the other hand, using the nitride-based InGaN/GaN QW system, these bandgaps can be accessible, as shown in Fig. 17. Hence, the growth of high quality of InGaN films with indium percentage that is higher than 20% is mandatory for next-generation six (or more) junctions. It should be mentioned that the values for the optimum bandgaps might change under high solar concentrations and this might open up new avenues for the use of different QW structures or designs [138].

By increasing the number of junctions in the multi-junction stack, there will be less current generated from each subcell. Comparing multi-junction solar cell devices based on four junction and seven junctions, the seven-junction device will exhibit a lower current and a higher voltage than the 4J device. Thus, it is important to guarantee that each subcell in next-generation five (or more) junction devices generates voltage close to the fundamental limit. To assess how close the solar cells to the fundamental limit set by Shockley–Quassier, the bandgap-voltage offset, $W_{oc} = E_g - V_{oc}$, is typically used as a figure of merit [139]. A W_{oc} close to 0.4 V indicates high internal radiative efficiency. QW solar cells, typically attain W_{oc} values close to 0.4 V. The InGaAs/GaAsP, shown in Fig. 8(a), has a W_{oc} value of 0.38 V. Similarly, the W_{oc} of the InGaAsP/InGaP, shown in Fig. 10(a), is 0.41 V. Thus, QWSC offer this advantage and can potentially be incorporated in multi-junction solar cells to

enhance the cell efficiency. It is also worth pointing out that some applications may require the high-temperature operation of solar cells such as hybrid photovoltaic-thermal systems that combine a PV cell to convert the high-energy photons to electricity and a thermal storage fluid to capture low-energy photons and use the dissipated heat in solar cell for power generation after sunset [140], [141]. Toward this goal, some researchers have investigated the effects of the high-temperature operation on the QWSC performance [142], [143]. For instance, Jeng *et al.* have reported on the degradation of the $In_{0.2}Ga_{0.8}N$/GaN QW solar cell efficiency to 0.79% at 340 °C as compared with 1.06% at room temperature. The reason behind the efficiency degradation is due to the reduction of reduction of V_{oc} [144] and possible reduction in the carrier lifetime and higher surface recombination velocity as the temperature is increased [141]. In addition, the carrier transport mechanisms such as thermionic emission or thermal-assisted tunneling are temperature-dependent processes as discussed in Section III-D. A more thorough understanding of the limiting factors of the high-temperature operation for QWSC is necessary for further performance improvements.

Beyond the use of QWs in solar cells, various QW structures and designs have also shown significant promise in other optoelectronic devices such as LEDs, modulators, photodiodes, and lasers.

VIII. Summary

In this paper, we have discussed the advantages and the challenges of epitaxial growth that governs the growth of high-performance QWSC. We studied three QW structures (InGaAs/GaAsP, InGaAsP/InGaP, InGaN/GaN) that have a high potential for future use in next-generation photovoltaic devices. For each material system, the bandgap tunability, critical layer thickness constraints, carrier transport mechanisms, and the criteria for realizing strain balance condition are discussed. We have reviewed some of the significant solar cells results of each structure and discussed the effect of well/barrier thickness on the light absorption and carrier collection. We have performed simulations that explain the effect of background doping on the electric field inside the QW region and the number of included QWs. The recent strategies to address the background doping such as sulfur/silicon compensation and the use of precursors that produce less carbon contamination is discussed. We have discussed the potential strategies that can be followed to enhance the QW external quantum efficiency of QWSC. The potential for incorporating QWs in next-generation multi-junction solar cell devices is discussed.

References

[1] D. M. Chapin, C. Fuller, and G. Pearson, "A new silicon p-n junction photocell for converting solar radiation into electrical power," *J. Appl. Phys.*, vol. 25, pp. 676–677, 1954.

[2] F. Dimroth *et al.*, "Wafer bonded four-junction GaInP/GaAs//GaInAsP/GaInAs concentrator solar cells with 44.7% efficiency," *Prog. Photovolt., Res. Appl.*, vol. 22, pp. 277–282, 2014.

[3] R. M. France *et al.*, "Design flexibility of ultrahigh efficiency four-junction inverted metamorphic solar cells," *IEEE J. Photovolt.*, vol. 6, no. 2, pp. 578–583, Mar. 2016.

[4] S. Bedair, M. Lamorte, and J. Hauser, "A two-junction cascade solar-cell structure," *Appl. Phys. Lett.*, vol. 34, pp. 38–39, 1979.

[5] N. Jain *et al.*, "High-efficiency inverted metamorphic 1.7/1.1 eV GaInAsP/GaInAs dual-junction solar cells," *Appl. Phys. Lett.*, vol. 112, 2018, Art. no. 053905.

[6] M. A. Green *et al.*, "Solar cell efficiency tables," *Prog. Photovolt., Res. Appl.*, vol. 25, pp. 668–676, 2018.

[7] M. A. Green, K. Emery, Y. Hishikawa, W. Warta, and E. D. Dunlop, "Solar cell efficiency tables (version 47)," *Prog. Photovolt., Res. Appl.*, vol. 24, pp. 3–11, 2016.

[8] T. Takamoto, H. Washio, and H. Juso, "Application of In-GaP/GaAs/InGaAs triple junction solar cells to space use and concentrator photovoltaic," in *Proc. IEEE 40th Photovolt. Spec. Conf.*, 2014, pp. 0001–0005.

[9] J. F. Geisz *et al.*, "Building a six-junction inverted metamorphic concentrator solar cell," *IEEE J. Photovolt.*, vol. 8, no. 2, pp. 626–632, Mar. 2018.

[10] J. F. Geisz *et al.*, "Six-junction concentrator solar cells," *AIP Conf. Proc.*, vol. 2012, 2018, Art. no. 040004.

[11] A. Luque, "Will we exceed 50% efficiency in photovoltaics?," *J. Appl. Phys.*, vol. 110, 2011, Art. no. 031301.

[12] C. H. Henry, "Limiting efficiencies of ideal single and multiple energy gap terrestrial solar cells," *J. Appl. Phys.*, vol. 51, pp. 4494–4500, 1980.

[13] N. G. Toledo and U. K. Mishra, "InGaN solar cell requirements for high-efficiency integrated III-nitride/non-III-nitride tandem photovoltaic devices," *J. Appl. Phys.*, vol. 111, 2012, Art. no. 114505.

[14] N. G. Toledo *et al.*, "Design of integrated III-nitride/non-III-nitride tandem photovoltaic devices," *J. Appl. Phys.*, vol. 111, 2012, Art. no. 054503.

[15] G. Letay, C. Baur, and A. Bett, "Theoretical investigations of III-V multijunction concentrator cells under realistic spectral conditions," in *Proc. 19th Eur. Photovolt. Sol. Energy Conf.*, 2004, pp. 11–15.

[16] G. B. Stringfellow, *Organometallic Vapor-Phase Epitaxy: Theory and Practice*. New York, NY, USA: Academic, 1999.

[17] H. Kressel, "The effect of crystal defects on optoelectronic devices," in *Semiconductors and Semimetals*, vol. 16. Amsterdam, The Netherlands: Elsevier, 1981, pp. 1–52.

[18] C. Andre *et al.*, "Impact of dislocations on minority carrier electron and hole lifetimes in GaAs grown on metamorphic SiGe substrates," *Appl. Phys. Lett.*, vol. 84, pp. 3447–3449, 2004.

[19] M. Yamaguchi and C. Amano, "Efficiency calculations of thin-film GaAs solar cells on Si substrates," *J. Appl. Phys.*, vol. 58, pp. 3601–3606, 1985.

[20] R. King *et al.*, "Next-generation, high-efficiency III-V multijunction solar cells," in *Proc. Conf. Rec. 28th IEEE Photovolt. Spec. Conf.*, 2000, pp. 998–1001.

[21] W. Guter *et al.*, "Current-matched triple-junction solar cell reaching 41.1% conversion efficiency under concentrated sunlight," *Appl. Phys. Lett.*, vol. 94, 2009, Art. no. 223504.

[22] I. Garcia *et al.*, "Metamorphic III–V solar cells: Recent progress and potential," *IEEE J. Photovolt.*, vol. 6, no. 1, pp. 366–373, Jan. 2016.

[23] R. M. France *et al.*, "Quadruple-junction inverted metamorphic concentrator devices," *IEEE J. Photovolt.*, vol. 5, no. 1, pp. 432–437, Jan. 2015.

[24] T. Katsuyama, S. Bedair, N. Giles, R. Burns, and J. Schetzina, "Growth and characterization of InGaAs/GaAsP strained layer superlattices," *J. Appl. Phys.*, vol. 62, pp. 498–502, 1987.

[25] H. Fujii *et al.*, "100-period, 1.23-eV bandgap InGaAs/GaAsP quantum wells for high-efficiency GaAs solar cells: Toward current-matched Ge-based tandem cells," *Prog. Photovolt., Res. Appl.*, vol. 22, pp. 784–795, 2013.

[26] K. Barnham and G. Duggan, "A new approach to high-efficiency multi-band-gap solar cells," *J. Appl. Phys.*, vol. 67, pp. 3490–3493, 1990.

[27] R. M. France *et al.*, "Multijunction solar cells with graded buffer bragg reflectors," *IEEE J. Photovolt.*, vol. 8, no. 6, pp. 1608–1615, Nov. 2018.

[28] T. Katsuyama *et al.*, "New approaches for high efficiency cascade solar cells," *Sol. Cells*, vol. 21, pp. 413–418, 1987.

[29] R. J. Chaffin and G. C. Osbourn, "Quantum well multijunction photovoltaic cell," U.S. Patent 4688068A, 1987.

[30] S. Adachi, "Material parameters of In1− x Ga x As y P1− y and related binaries," *J. Appl. Phys.*, vol. 53, pp. 8775–8792, 1982.

[31] J. Adams *et al.*, "Recent results for single-junction and tandem quantum well solar cells," *Prog. Photovolt., Res. Appl.*, vol. 19, pp. 865–877, 2011.

[32] G. K. Bradshaw *et al.*, "Carrier transport and improved collection in thin-barrier InGaAs/GaAsP strained quantum well solar cells," *IEEE J. Photovolt.*, vol. 3, no. 1, pp. 278–283, Jan. 2013.

[33] S. Bedair, T. Katsuyama, M. Timmons, and M. Tischler, "A new GaAsP—InGaAs strained-layer super-lattice light-emitting diode," *IEEE Electron Device Lett.*, vol. 5, no. 2, pp. 45–47, Feb. 1984.

[34] N. Ekins-Daukes *et al.*, "Strain-balanced GaAsP/InGaAs quantum well solar cells," *Appl. Phys. Lett.*, vol. 75, pp. 4195–4197, 1999.

[35] K.-H. Lee *et al.*, "Demonstration of photon coupling in dual multiple-quantum-well solar cells," *IEEE J. Photovolt.*, vol. 2, no. 1, pp. 68–74, Jan. 2012.

[36] R. Hoheisel *et al.*, "Quantum-well solar cells for space: The impact of carrier removal on end-of-life device performance," *IEEE J. Photovolt.*, vol. 4, no. 1, pp. 253–259, Jan. 2014.

[37] K. Toprasertpong *et al.*, "Absorption threshold extended to 1.15 eV using InGaAs/GaAsP quantum wells for over-50%-efficient lattice-matched quad-junction solar cells," *Prog. Photovolt., Res. Appl.*, vol. 24, pp. 533–542, 2016.

[38] D. Alonso-Álvarez *et al.*, "InGaAs/GaAsP strain balanced multi-quantum wires grown on misoriented GaAs substrates for high efficiency solar cells," *Appl. Phys. Lett.*, vol. 105, 2014, Art. no. 083124.

[39] G. K. Bradshaw *et al.*, "GaInP/GaAs tandem solar cells with In-GaAs/GaAsP multiple quantum wells," *IEEE J. Photovolt.*, vol. 4, no. 2, pp. 614–619, Mar. 2014.

[40] H. Fujii, Y. Wang, K. Watanabe, M. Sugiyama, and Y. Nakano, "High-aspect-ratio structures for efficient light absorption and carrier transport in InGaAs/GaAsP multiple quantum well solar cells," in *Proc. 2012 IEEE 38th Photovolt. Spec. Conf.*, 2012, pp. 1–9.

[41] I. E. Sayed, N. Jain, M. A. Steiner, J. F. Geisz, and S. Bedair, "100-period InGaAsP/InGaP superlattice solar cell with sub-bandgap quantum efficiency approaching 80%," *Appl. Phys. Lett.*, vol. 111, 2017, Art. no. 082107.

[42] I. E. H. Sayed, C. Z. Carlin, B. G. Hagar, P. C. Colter, and S. Bedair, "Strain-balanced InGaAsP/GaInP multiple quantum well solar cells with a tunable bandgap (1.65–1.82 eV)," *IEEE J. Photovolt.*, vol. 6, no. 4, pp. 997–1003, Jul. 2016.

[43] I. E. Hashem, C. Zachary Carlin, B. G. Hagar, P. C. Colter, and S. M. Bedair, "InGaP-based quantum well solar cells: Growth, structural design, and photovoltaic properties," *J. Appl. Phys.*, vol. 119, 2016, Art. no. 095706.

[44] R. Dahal, B. Pantha, J. Li, J. Lin, and H. Jiang, "InGaN/GaN multiple quantum well solar cells with long operating wavelengths," *Appl. Phys. Lett.*, vol. 94, 2009, Art. no. 063505.

[45] R. Dahal, J. Li, K. Aryal, J. Lin, and H. Jiang, "InGaN/GaN multiple quantum well concentrator solar cells," *Appl. Phys. Lett.*, vol. 97, 2010, Art. no. 073115.

[46] K. Lai, G. Lin, Y.-L. Lai, Y. Chen, and J. He, "Effect of indium fluctuation on the photovoltaic characteristics of InGaN/GaN multiple quantum well solar cells," *Appl. Phys. Lett.*, vol. 96, 2010, Art. no. 081103.

[47] R. M. Farrell *et al.*, "High quantum efficiency InGaN/GaN multiple quantum well solar cells with spectral response extending out to 520 nm," *Appl. Phys. Lett.*, vol. 98, 2011, Art. no. 201107.

[48] D. Van Den Broeck, D. Bharrat, A. Hosalli, N. El-Masry, and S. Bedair, "Strain-balanced InGaN/GaN multiple quantum wells," *Appl. Phys. Lett.*, vol. 105, 2014, Art. no. 031107.

[49] J. Bai, Y. Gong, Z. Li, Y. Zhang, and T. Wang, "Semi-polar InGaN/GaN multiple quantum well solar cells with spectral response at up to 560nm," *Sol. Energy Mater. Sol. Cells*, vol. 175, pp. 47–51, 2018.

[50] X. Huang *et al.*, "Energy band engineering of InGaN/GaN multi-quantum-well solar cells via AlGaN electron-and hole-blocking layers," *Appl. Phys. Lett.*, vol. 113, 2018, Art. no. 043501.

[51] P. Harrison, *Quantum Wells, Wires and Dots: Theoretical and Computational Physics of Semiconductor Nanostructures*, Hoboken, NJ, USA: Wiley, 2005.

[52] G. Bastard, E. Mendez, L. Chang, and L. Esaki, "Variational calculations on a quantum well in an electric field," *Phys. Rev. B*, vol. 28, 1983, Art. no. 3241.

[53] M. Buongiorno Nardelli, K. Rapcewicz, and J. Bernholc, "Polarization field effects on the electron-hole recombination dynamics in In 0.2 Ga 0.8 N/In 1− x Ga x N multiple quantum wells," *Appl. Phys. Lett.*, vol. 71, pp. 3135–3137, 1997.

[54] S. Adachi, "Material parameters of In1− xGaxAsyP1− y and related binaries," *J. Appl. Phys.*, vol. 53, pp. 8775–8792, 1982.

[55] R. Anderson, "Germanium-gallium arsenide heterojunctions [letter to the editor]," *IBM J. Res. Develop.*, vol. 4, pp. 283–287, 1960.

[56] H. Asai and K. Oe, "Energy band-gap shift with elastic strain in Ga x In1− x P epitaxial layers on (001) GaAs substrates," *J. Appl. Phys.*, vol. 54, pp. 2052–2056, 1983.

[57] B. A. Foreman, "Analytic model for the valence-band structure of a strained quantum well," *Phys. Rev. B*, vol. 49, pp. 1757–1773, 1994.

[58] S. Essig *et al.*, "Progress towards a 30% efficient GaInP/Si tandem solar cell," *Energy Procedia*, vol. 77, pp. 464–469, 2015.

[59] A. G. Bhuiyan, K. Sugita, A. Hashimoto, and A. Yamamoto, "InGaN solar cells: Present state of the art and important challenges," *IEEE J. Photovolt.*, vol. 2, no. 3, pp. 276–293, Jul. 2012.

[60] J. Matthews and A. Blakeslee, "Defects in epitaxial multilayers: I. Misfit dislocations," *J. Crystal Growth*, vol. 27, pp. 118–125, 1974.

[61] J. Matthews and A. Blakeslee, "Defects in epitaxial multilayers: III. Preparation of almost perfect multilayers," *J. Crystal Growth*, vol. 32, pp. 265–273, 1976.

[62] D. Holec *et al.*, "Equilibrium critical thickness for misfit dislocations in III-nitrides," *J. Appl. Phys.*, vol. 104, 2008, Art. no. 123514.

[63] C. Parker *et al.*, "Determination of the critical layer thickness in the InGaN/GaN heterostructures," *Appl. Phys. Lett.*, vol. 75, pp. 2776–2778, 1999.

[64] M. Reed, N. El-Masry, C. Parker, J. Roberts, and S. Bedair, "Critical layer thickness determination of GaN/InGaN/GaN double heterostructures," *Appl. Phys. Lett.*, vol. 77, pp. 4121–4123, 2000.

[65] X. Li *et al.*, "Minimized open-circuit voltage reduction in GaAs/InGaAs quantum well solar cells with bandgap-engineered graded quantum well depths," *Appl. Phys. Lett.*, vol. 105, 2014, Art. no. 123906.

[66] N. Ekins-Daukes, K. Kawaguchi, and J. Zhang, "Strain-balanced criteria for multiple quantum well structures and its signature in X-ray rocking curves," *Crystal Growth Design*, vol. 2, pp. 287–292, 2002.

[67] J. Nelson, M. Paxman, K. Barnham, J. Roberts, and C. Button, "Steady-state carrier escape from single quantum wells," *IEEE J. Quantum Electron.*, vol. 29, no. 6, pp. 1460–1468, Jun. 1993.

[68] H. Schneider and K. V. Klitzing, "Thermionic emission and Gaussian transport of holes in a GaAs/Al x Ga 1− x As multiple-quantum-well structure," *Phys. Rev. B*, vol. 38, pp. 6160–6165, 1988.

[69] D. A. Miller, G. Livescu, J. Cunningham, and W. Y. Jan, "Quantum well carrier sweep out: Relation to electroabsorption and exciton saturation," *IEEE J. Quantum Electron.*, vol. 27, no. 10, pp. 2281–2295, Oct. 1991.

[70] G. K. Bradshaw, "Characterization and analysis of multi-quantum well solar cells," *Ph.D. dissertation*, North Carolina State Univ., Raleigh, NC, USA, 2014.

[71] B. F. Moody, "Strained layer superlattice solar cells," *Ph.D. dissertation*, North Carolina State Univ., Raleigh, NC, USA, 2007.

[72] G. K. Bradshaw *et al.*, "Effects of barrier width on spectral response of strained layer superlattices for high efficiency solar cells," *MRS Online Library Archive*, vol. 1211, pp. R02–R08, 2009.

[73] B. Miller *et al.*, "High quality narrow GaInAs/InP quantum wells grown by atmospheric organometallic vapor phase epitaxy," *Appl. Phys. Lett.*, vol. 49, pp. 1384–1386, 1986.

[74] T. Wang, E. Reihlen, H. Jen, and G. Stringfellow, "Systematic studies on the effect of growth interruptions for GaInAs/InP quantum wells grown by atmospheric pressure organometallic vapor-phase epitaxy," *J. Appl. Phys.*, vol. 66, pp. 5376–5383, 1989.

[75] C.-Y. Lee, M.-C. Wu, H.-P. Shiao, T.-T. Shi, and W.-J. Ho, "MOCVD growth of strained multiple quantum well structure for 1.3 μm InAsP/InP laser diodes," *Solid-State Electron.*, vol. 43, pp. 2141–2146, 1999.

[76] J. Samberg, C. Carlin, G. Bradshaw, P. Colter, and S. Bedair, "Growth and characterization of InxGa1− xAs/GaAs1− yPy strained-layer superlattices with high values of y (∼80%)," *J. Electron. Mater.*, vol. 42, pp. 912–917, 2013.

[77] J. P. Samberg *et al.*, "Interface properties of Ga (As, P)/(In, Ga) As strained multiple quantum well structures," *Appl. Phys. Lett.*, vol. 103, 2013, Art. no. 071605.

[78] Y. Wen, Y. Wang, and Y. Nakano, "Suppressed indium diffusion and enhanced absorption in InGaAs/GaAsP stepped quantum well solar cell," *Appl. Phys. Lett.*, vol. 100, 2012, Art. no. 053902.

[79] D. Bushnell *et al.*, "Effect of well number on the performance of quantum-well solar cells," *J. Appl. Phys.*, vol. 97, 2005, Art. no. 124908.

[80] I. E. H. Sayed, C. Z. Carlin, B. Hagar, P. C. Colter, and S. M. Bedair, "Tunable GaInP solar cell lattice matched to GaAs," in *Proc. IEEE 42nd Photovolt. Spec. Conf.*, 2015, pp. 1–4.

[81] N. Jain, J. F. Geisz, R. M. France, A. G. Norman, and M. A. Steiner, "Enhanced current collection in 1.7 eV GaInAsP solar cells grown on GaAs by metalorganic vapor phase epitaxy," *IEEE J. Photovolt.*, vol. 7, no. 3, pp. 927–933, May 2017.

[82] G. Erbert *et al.*, "High-power tensile-strained GaAsP-AlGaAs quantum-well lasers emitting between 715 and 790 nm," *IEEE J. Sel. Topics Quantum Electron.*, vol. 5, no. 3, pp. 780–784, May/Jun. 1999.

[83] A. Al-Muhanna, J. Wade, L. Mawst, and R. Fu, "730-nm-emitting Al-free active-region diode lasers with compressively strained InGaAsP quantum wells," *Appl. Phys. Lett.*, vol. 72, 1998, Art. no. 641.

[84] D. Z. Garbuzov *et al.*, "High-power 0. 8. mu. m InGaAsP-GaAs SCH SQW lasers," *IEEE J. Quantum Electron.*, vol. 27, no. 6, pp. 1531–1536, Jun. 1991.

[85] F. Yam and Z. Hassan, "Innovative advances in LED technology," *Microelectron. J.*, vol. 36, pp. 129–137, 2005.

[86] F. M. Steranka, "AlGaAs red light-emitting diodes," *Semicond. Semimetals*, vol. 48, pp. 65–96, 1997.

[87] Y. Konaka, K.-I. Ono, Y. Terai, and Y. Fujiwara, "Coexistence properties of phase separation and CuPt-ordering in InGaAsP grown on GaAs substrates by organometallic vapor phase epitaxy," *J. Crystal Growth*, vol. 312, pp. 2056–2059, 2010.

[88] J. F. Geisz, M. A. Steiner, I. Garcia, S. R. Kurtz, and D. J. Friedman, "Enhanced external radiative efficiency for 20.8% efficient single-junction GaInP solar cells," *Appl. Phys. Lett.*, vol. 103, 2013, Art. no. 041118.

[89] G. Stringfellow, "Immiscibility and spinodal decomposition in III/V alloys," *J. Crystal Growth*, vol. 65, pp. 454–462, 1983.

[90] K. Onabe, "Calculation of miscibility gap in quaternary InGaPAs with strictly regular solution approximation," *Jpn. J. Appl. Phys.*, vol. 21, 1982, Art. no. 797.

[91] T. Kato, T. Matsumoto, T. Kobatake, and T. Ishida, "Strain-energy-stabilized growth of InGaAsP layers on GaAs (111) A substrates in immiscible region," *Jpn. J. Appl. Phys.*, vol. 26, 1987, Art. no. L1161.

[92] I. E. Sayed *et al.*, "In-situ curvature monitoring and X-ray diffraction study of InGaAsP/InGaP quantum wells," *J. Crystal Growth*, vol. 475, pp. 171–177, 2017.

[93] N. Jain *et al.*, "Development of lattice-matched 1.7 eV GaInNAsP solar cells grown on GaAs by MOVPE," in *Proc. IEEE 43rd Photovolt. Spec. Conf.*, 2016, pp. 0046–0051.

[94] E. Berkman, N. El-Masry, A. Emara, and S. Bedair, "Nearly lattice-matched n, i, and p layers for InGaN p-i-n photodiodes in the 365–500 nm spectral range," *Appl. Phys. Lett.*, vol. 92, 2008, Art. no. 101118.

[95] J. Wu *et al.*, "Superior radiation resistance of In 1− x Ga x N alloys: Full-solar-spectrum photovoltaic material system," *J. Appl. Phys.*, vol. 94, pp. 6477–6482, 2003.

[96] L. Hsu and W. Walukiewicz, "Modeling of InGaN/Si tandem solar cells," *J. Appl. Phys.*, vol. 104, 2008, Art. no. 024507.

[97] C. J. Neufeld *et al.*, "Effect of doping and polarization on carrier collection in InGaN quantum well solar cells," *Appl. Phys. Lett.*, vol. 98, 2011, Art. no. 243507.

[98] J. Wierer, Jr., A. Fischer, and D. Koleske, "The impact of piezoelectric polarization and nonradiative recombination on the performance of (0001) face GaN/InGaN photovoltaic devices," *Appl. Phys. Lett.*, vol. 96, 2010, Art. no. 051107.

[99] J. Wierer, Jr., D. Koleske, and S. R. Lee, "Influence of barrier thickness on the performance of InGaN/GaN multiple quantum well solar cells," *Appl. Phys. Lett.*, vol. 100, 2012, Art. no. 111119.

[100] J. Lang, N. Young, R. M. Farrell, Y.-R. Wu, and J. Speck, "Carrier escape mechanism dependence on barrier thickness and temperature in InGaN quantum well solar cells," *Appl. Phys. Lett.*, vol. 101, 2012, Art. no. 181105.

[101] S.-B. Choi *et al.*, "Effect of indium composition on carrier escape in InGaN/GaN multiple quantum well solar cells," *Appl. Phys. Lett.*, vol. 103, 2013, Art. no. 033901.

[102] S. J. Pearton, *GaN and Related Materials II*, vol. 7. Boca Raton, FL, USA: CRC Press, 2000.

[103] I. H. Ho and G. Stringfellow, "Solid phase immiscibility in GaInN," *Appl. Phys. Lett.*, vol. 69, pp. 2701–2703, 1996.

[104] M. Behbehani, E. Piner, S. Liu, N. El-Masry, and S. Bedair, "Phase separation and ordering coexisting in In x Ga 1− x N grown by metal organic chemical vapor deposition," *Appl. Phys. Lett.*, vol. 75, pp. 2202–2204, 1999.

[105] D. Van Den Broeck, D. Bharrat, Z. Liu, N. El-Masry, and S. Bedair, "Growth and characterization of high-quality, relaxed InyGa1−yN templates for optoelectronic applications," *J. Electron. Mater.*, vol. 44, pp. 4161–4166, 2015.

[106] D. M. Van Den Broeck, "Engineering strain for improved III-Nitride optoelectronic device performance," *Ph.D. dissertation*, North Carolina State Univ., Raleigh, NC, USA, 2016.

[107] S. Yamasaki *et al.*, "P-type conduction in Mg-doped Ga0. 91In0. 09N grown by metalorganic vapor-phase epitaxy," *Appl. Phys. Lett.*, vol. 66, pp. 1112–1113, 1995.

[108] K. Kumakura, T. Makimoto, and N. Kobayashi, "Activation energy and electrical activity of Mg in Mg-doped InxGa1-xN (x< 0.2)," *Jpn. J. Appl. Phys.*, vol. 39, 2000, Art. no. L337.

[109] R. King *et al.*, "Pathways to 40%-efficient concentrator photovoltaics," in *Proc. 20th Eur. Photovolt. Sol. Energy Conf.*, 2005, pp. 10–11.

[110] S. Heckelmann, D. Lackner, C. Karcher, F. Dimroth, and A. W. Bett, "Investigations on Al Ga As solar cells grown by MOVPE," *IEEE J. Photovolt.*, vol. 5, no. 1, pp. 446–453, Jan. 2015.

[111] S. Bedair, J. L. Harmon, C. Z. Carlin, I. E. H. Sayed, and P. Colter, "High performance as-grown and annealed high band gap tunnel junctions: Te behavior at the interface," *Appl. Phys. Lett.*, vol. 108, 2016, Art. no. 203903.

[112] S. M. Bedair, J. L. Harmon, C. Z. Carlin, I. E. H. Sayed, and P. Colter, "Annealed high band gap tunnel junctions with peak current densities above 800 A/cm 2," in *Proc. IEEE 43rd Photovolt. Spec. Conf.*, 2016, pp. 2320–2322.

[113] S. Bedair, C. Z. Carlin, J. L. Harmon, I. E. H. Sayed, and P. Colter, "High performance tunnel junction with resistance to thermal annealing," *AIP Conf. Proc.*, vol. 1766, 2016, Art. no. 020003.

[114] M. Kondo *et al.*, "Origin of nonradiative recombination centers in Al-GaInP grown by metalorganic vapor phase epitaxy," *J. Electron. Mater.*, vol. 23, pp. 355–358, 1994.

[115] M. Kondo *et al.*, "Crystallographic orientation dependence of impurity incorporation into III-V compound semiconductors grown by metalorganic vapor phase epitaxy," *J. Appl. Phys.*, vol. 76, pp. 914–927, 1994.

[116] E. E. Perl *et al.*, "Development of a 2.0 eV AlGaInP solar cell grown by OMVPE," in *Proc. IEEE 42nd Photovolt. Spec. Conf.*, 2015, pp. 1–6.

[117] E. E. Perl *et al.*, "Development of high-bandgap AlGaInP solar cells grown by organometallic vapor-phase epitaxy," *IEEE J. Photovolt.*, vol. 6, no. 3, pp. 770–776, May 2016.

[118] S. Maximenko *et al.*, "Radiation response of multi-quantum well solar cells: Electron-beam-induced current analysis," *J. Appl. Phys.*, vol. 118, 2015, Art. no. 245705.

[119] M. Gonzalez *et al.*, "Radiation study in quantum well III-V multi-junction solar cells," in *Proc. IEEE 39th Photovolt. Spec. Conf.*, 2013, pp. 3233–3236.

[120] R. Kellenbenz *et al.*, "Development of radiation hard Ga 0.50 In 0.50 P/Ga 0.99 In 0.01 As/Ge space solar cells with multi quantum wells," in *Proc. 35th IEEE Photovolt. Spec. Conf.*, 2010, pp. 000117–000122.

[121] N. Ekins-Daukes *et al.*, "Carrier removal in lattice-mismatched InGaP solar cells under 1-MeV-electron irradiation," *Appl. Phys. Lett.*, vol. 85, pp. 2511–2513, 2004.

[122] D. A. Clugston and P. A. Basore, "PC1D version 5: 32-bit solar cell modeling on personal computers," in *Proc. Conf. Rec. 26th IEEE Photovolt. Spec. Conf.*, 1997, pp. 207–210.

[123] D. E. Aspnes, "Optical properties of thin films," *Thin Solid Films*, vol. 89, pp. 249–262, 1982.

[124] K. Driscoll, M. F. Bennett, S. J. Polly, D. V. Forbes, and S. M. Hubbard, "Effect of quantum dot position and background doping on the performance of quantum dot enhanced GaAs solar cells," *Appl. Phys. Lett.*, vol. 104, 2014, Art. no. 023119.

[125] J. Nelson *et al.*, "Effect of quantum well location on single quantum well pin photodiode dark currents," *J. Appl. Phys.*, vol. 86, pp. 5898–5905, 1999.

[126] M. Sugiyama, Y. Wang, S. Choi, Y. Wen, and Y. Nakano, "How shall we put multiple quantum wells in pin structure for efficiency enhancement?," in *Proc. 35th IEEE Photovolt. Spec. Conf.*, 2010, pp. 000376–000379.

[127] H. Fujii, Y. Wang, K. Watanabe, M. Sugiyama, and Y. Nakano, "Compensation doping in InGaAs/GaAsP multiple quantum well solar cells for efficient carrier transport and improved cell performance," *J. Appl. Phys.*, vol. 114, 2013, Art. no. 103101.

[128] H. Fujii *et al.*, "InGaAs/GaAsP superlattice solar cells with reduced carbon impurity grown by low-temperature metal-organic vapor phase epitaxy using triethylgallium," *J. Appl. Phys.*, vol. 116, 2014, Art. no. 203101.

[129] T. Kuech and J. Redwing, "Carbon doping in metalorganic vapor phase epitaxy," *J. Crystal Growth*, vol. 145, pp. 382–389, 1994.

[130] T. Kuech and R. Potemski, "Reduction of background doping in metalorganic vapor phase epitaxy of GaAs using triethylgallium at low reactor pressures," *Appl. Phys. Lett.*, vol. 47, pp. 821–823, 1985.

[131] M. Yoshida, H. Watanabe, and F. Uesugi, "Mass spectrometric study of Ga(CH₃)₃ and Ga(C₂H₅)₃ decomposition reaction in H₂ and N₂," *J. Electrochem. Soc.*, vol. 132, no. 3, pp. 677–679, 1985.

[132] N. Kobayashi and T. Makimoto, "Reduced carbon contamination in OMVPE grown GaAs and AlGaAs," *Jpn. J. Appl. Phys.*, vol. 24, 1985, Art. no. L824.

[133] D. K. Russell, "Gas-Phase pyrolysis mechanisms in organometallic CVD," *Chemical Vapor Deposition*, vol. 2, pp. 223–233, 1996.

[134] M. Pristovsek, M. Zorn, and M. Weyers, "In situ study of GaAs growth mechanisms using tri-methyl gallium and tri-ethyl gallium precursors in metal-organic vapour phase epitaxy," *J. Crystal Growth*, vol. 262, pp. 78–83, 2004.

[135] J. A. Floro and E. Chason, "Curvature based techniques for realtime stress measurements during thin film growth," in *In-Situ Characterization of Thin Film Growth Processes*. Hoboken, NJ, USA: Wiley, 2001, p. 191.

[136] Y. Wang *et al.*, "In situ reflectance monitoring for the MOVPE of strain-balanced InGaAs/GaAsP quantum-wells," *J. Crystal Growth*, vol. 312, pp. 1364–1369, 2010.

[137] Y. P. Wang, S. J. Ma, K. Watanabe, M. Sugiyama, and Y. Nakano, "Management of highly-strained heterointerface in InGaAs/GaAsP strain-balanced superlattice for photovoltaic application," *J. Crystal Growth*, vol. 352, pp. 194–198, 2012.

[138] S. Bremner, M. Levy, and C. B. Honsberg, "Analysis of tandem solar cell efficiencies under AM1. 5G spectrum using a rapid flux calculation method," *Prog. Photovolt., Res. Appl.*, vol. 16, pp. 225–233, 2008.

[139] R. King *et al.*, "Band gap-voltage offset and energy production in next-generation multijunction solar cells," *Prog. Photovolt., Res. Appl.*, vol. 19, pp. 797–812, 2011.

[140] H. M. Branz *et al.*, "Hybrid solar converters for maximum exergy and inexpensive dispatchable electricity," *Energy Environ. Sci.*, vol. 8, pp. 3083–3091, 2015.

[141] E. Perl, D. Kuciauskas, J. Simon, D. J. Friedman, and M. A. Steiner, "Identification of the limiting factors for high-temperature GaAs, GaInP, and AlGaInP solar cells from device and carrier lifetime analysis," *J. Appl. Phys.*, vol. 122, 2017, Art. no. 233102.

[142] M.-J. Jeng, Y.-L. Lee, and L.-B. Chang, "Temperature dependences of InxGa1− xN multiple quantum well solar cells," *J. Phys. D, Appl. Phys.*, vol. 42, 2009, Art. no. 105101.

[143] D.-H. Lien *et al.*, "Harsh photovoltaics using InGaN/GaN multiple quantum well schemes," *Nano Energy*, vol. 11, pp. 104–109, 2015.

[144] J. C. C. Fan, "Theoretical temperature dependence of solar cell parameters," *Sol. Cells*, vol. 17, pp. 309–315, 1986.

Authors' photographs and biographies not available at the time of publication.